

A multiwavelength study of the S 106 region

II. Characteristics of the photon dominated region[★]

N. Schneider^{1,2,3}, R. Simon^{1,4}, C. Kramer¹, K. Kraemer⁴, J. Stutzki¹, and B. Mookerjea¹

¹ I. Physikalisches Institut, Universität zu Köln, Zùlpicher Straße 77, 50937 Köln, Germany

² IRAM and Observatoire de Grenoble, BP 53, 38406 Saint Martin d'Hères, France

³ Observatoire de Bordeaux, BP 89, 33270 Floirac, France

⁴ Institute for Astrophysical Research, Boston University, 725 Commonwealth Avenue, Boston, MA 02215, USA

Received 11 October 2002 / Accepted 6 May 2003

Abstract. The O star S 106 IR powers a bright, spatially extended $10' \times 3'$ (1.75×0.5 pc at a distance of 600 pc) photon dominated region (PDR) traced by our observations of FIR fine structure lines and submm molecular transitions. The [C II] 158 μm , [C I] 609 and 370 μm , CO 7 \rightarrow 6, and CO 4 \rightarrow 3 measurements probe the large scale (1.2 pc) PDR emission, whereas [O I] 63 μm , CN $N = 3\rightarrow 2$, and CS $J = 7\rightarrow 6$ observations are focused on the immediate ($\sim 1'$ (0.2 pc)) environment of S 106 IR. A hot ($T > 200$ K) and dense ($n > 3 \times 10^5 \text{ cm}^{-3}$) gas component (emission peaks of [C II] 158 μm , CO 7 \rightarrow 6, and CO 4 \rightarrow 3) is found at S 106 IR. Cooler gas associated with the bulk emission of the molecular cloud is characterized by two emission peaks (one close (20'' east) to S 106 IR and one 120'' to the west) seen in the [C I] and low- J ($J_{\text{up}} < 4$) CO emission lines. In the immediate environment of the star, the molecular and [C I] lines show high-velocity emission due to the interaction of the cloud with the stellar wind of S 106 IR.

The intensities of the FIR lines measured with the KAO are compared to those observed with the ISO LWS towards two positions, S 106 IR and 120'' west. We discuss intensities and line ratios of the observed species along a cut through the molecular cloud/H II region interface centered on S 106 IR. The excitation conditions (T_{ex} , opacities, column densities) are derived from an LTE analysis. We find that the temperature at the position of S 106 IR obtained from the [C I] excitation is high (> 500 K), resulting in substantial population of the energetically higher $^3\text{P}_2$ state; the analysis of the mid- and high- J CO excitation confirms the higher temperature at S 106 IR. At this position, the [O I] 63 μm line is the most important cooling line, followed by other atomic FIR lines ([O III] 52 μm , [C II] 158 μm) and high- J CO lines, which are more efficient coolants compared to [C I] 2 \rightarrow 1 and 1 \rightarrow 0. We compare the observed line ratios to plane-parallel PDR model predictions and obtain consistent results for UV fluxes spanning a range from 10^2 to $10^{3.5} G_0$ and densities around 10^5 cm^{-3} only at positions away from S 106 IR. Towards S 106 IR, we estimate a density of at least 3×10^5 at temperatures between 200 and 500 K from non-LTE modelling of the CO 16 \rightarrow 15/14 \rightarrow 13 ratio and the CO 7 \rightarrow 6 intensity. Our new observations support the picture drawn in the first part of this serie of papers that high-density ($n > 10^5 \text{ cm}^{-3}$) clumps with a hot PDR surface are embedded in low- to medium density gas ($n \leq 10^4 \text{ cm}^{-3}$).

Key words. ISM: atoms – ISM: clouds – ISM: individual objects: S 106 – ISM: structure – radio lines: ISM

1. Introduction

Sharpless 106 is a bipolar H II region with an obscuring dust lane perpendicular to the ionized lobes, embedded in an extended molecular cloud (Bally & Scoville 1982). The H II region is excited by a single O7–O9 star (Eiroa et al. 1979; Gehrz et al. 1982), which also provides the UV flux to power a bright photon dominated region (PDR) at the interface to

the surrounding molecular cloud. The central star is referred to as S 106 IR (Richer et al. 1993), other names include S 106 IRS 3, IRS 4 and S 106 PS. A cluster of 160 stars, detected by Hodapp & Rayner (1991), surrounds S 106 IR within a radius of 1'.7, which is equivalent to 0.3 pc at a distance of 600 pc (Staude et al. 1982).

The molecular cloud surrounding the H II region has been investigated using various molecular line tracers over a broad range of angular resolutions (typically 10''–15'' for interferometric data and up to several arcmin for extended low- J ($J_{\text{up}} < 4$) CO maps). The observations revealed a molecular cloud with 20' \times 25' (3.5×4.4 pc) extent. Maps in optically thin

Send offprint requests to: N. Schneider,
e-mail: schneider@obs.u-bordeaux1.fr

[★] Appendix A is only available in electronic form at
<http://www.edpsciences.org>

lines of NH₃ (Stutzki et al. 1982) and ¹³CO (Bally & Scoville 1982; Schneider et al. 2002), show two emission peaks, separated by 3'.

Continuum maps of dust emission at 1300 and 350 μm (Mezger et al. 1987) and 1100, 800, and 450 μm (Richer et al. 1993), show a double peak emission distribution on a smaller scale with two peaks located 15'' east and west of S 106 IR. A pronounced western peak (S 106 FIR) at 450 μm is interpreted by Richer et al. (1993) as a Class 0 object since it coincides with a region of H₂O masers (Stutzki et al. 1982; Furuya et al. 1999). A good correspondence between dust and molecular gas emission is seen in the interferometric HCO⁺ $J = 1 \rightarrow 0$ map of Loushin et al. (1990), whereas the interferometric HCN $J = 1 \rightarrow 0$ map of Kaifu (1985) anticorrelates with the cold dust.

Observations of the cloud in lines specifically tracing PDR gas were first performed by Harris et al. (1987) (¹²CO $J = 7 \rightarrow 6$ and ¹²CO $J = 14 \rightarrow 13$), followed by Graf et al. (1993) and Richer et al. (1993), who studied selected positions in the ¹²CO and ¹³CO $J = 6 \rightarrow 5$ lines at an angular resolution of 8'' at the JCMT, and Little et al. (1995) ([C I] 809 μm fine structure line). In particular the detection of medium- J ($4 \leq J_{\text{up}} \leq 6$) to high- J ($J_{\text{up}} > 6$) CO lines indicate the presence of warm ($T > 100$ K) and at least medium dense ($n > 10^4$ cm⁻³) gas close to S 106 IR (Harris et al. 1987).

All these observations concentrated on the PDR immediately surrounding S 106 IR and did not show the full extent of the UV influenced gas. Our larger scale (1.2 pc) mapping of the [C II] 158 μm, [C I] 809 and 370 μm, and CO 7→6 and 4→3 lines are intended to reveal the whole spatial extent of the PDR region, while higher angular resolution [O I] observations provide a more detailed view of the higher density PDR gas. The purpose of the present work is to study the impact of FUV radiation from a single, massive O star on its molecular environment.

It is now generally accepted that the observed *extended* [C II] emission in star forming regions (e.g., M 17, Stutzki et al. 1988; Rosette, Schneider et al. 1998; W 3, NGC 1977, NGC 2023, Howe et al. 1991) and the mid- J ¹³CO emission (Graf et al. 1993; models by Köster et al. 1994) can only be explained with a highly fragmented cloud structure, enabling a large penetration depth of UV photons. Some authors model the observed PDR line emission distributions and intensities with two- or three phase models (M 17, Meixner et al. 1992; W 51, W 49, Jaffe et al. 1987). Observational evidence for the existence of predominantly homogeneous gas (but including a small number of embedded very dense clumps) on small length scales was found by Tauber et al. (1994) and Hogerheijde et al. (1995) for the Orion Bar. A similar conclusion was drawn by Schneider et al. (2002) for S 106 from observations of low and medium- J CO lines. Accordingly, depending on the degree of fragmentation and the clump/interclump gas contrast, plane-parallel, homogeneous PDR models fail to explain a full set of observed (sub)mm- and FIR intensities and ratios or can only be successfully applied to lines tracing a specific regime of physical parameters (for example the [O I] FIR lines and the high- J CO lines, which are tracers of high-density and high-temperature gas).

The paper is organized as follows: Sect. 2 describes the observations of the FIR and molecular lines, which are presented in Sect. 3. In Sect. 4, we discuss the observed line intensities along a cut through the molecular cloud and PDR region. A homogeneous, plane-parallel PDR model, incorporating the FIR line intensities and ratios and additional CO data, is used to derive the particle density and the incident UV flux in Sect. 5. Section 6 summarizes the paper.

2. Observations

The fine structure and molecular line maps obtained for this work are centred on the position of the star S 106 IR at RA(B1950.0) = 20^h25^m33.8^s and DEC(B1950.0) = 37°12'50''. This will be referred to as the (0,0) position (the same used for all figures in Schneider et al. 2002) and marked by a star in the figures of the paper.

2.1. [C II] and [O I] atomic fine structure lines

The observations of the [C II] 157.7409 μm and [O I] 63.1837 μm fine structure lines in S 106 were carried out in 1994 June with the MPE/UCB Fabry-Perot Interferometer FIFI (Poglitsch et al. 1991) onboard the NASA Kuiper Airborne Observatory.

For the [O I] 63 μm observations, the 5 × 5 focal plane detector array was centered on the exciting star S 106 IR. The pixel-to-pixel spacing was 20'' and the effective angular resolution 22''. The Lorentzian instrument profile has a velocity resolution of 64 km s⁻¹ so that the [O I] line is not spectrally resolved. The observations were taken in the “scanning” mode of FIFI with a chop throw of 6' in N-S direction. The system Noise Equivalent Power (NEP) during the flight was 1.36 × 10⁻¹⁴ W Hz^{-1/2}.

For the [C II] 158 μm observations, the array was also centered on S 106 IR. Two additional settings were taken in the [C II] line west and east of S 106 IR at (-200'', 0) and (200'', 0). Here, the spacing between the pixels was 40'' and the angular resolution 55''. FIFI was operated in the “scanning mode” with a chop throw of 7' in N-S. The velocity resolution is 49 km s⁻¹.

All data were flat-fielded and calibrated by dividing by scans taken on internal blackbodies. The integrated line intensities were derived by fitting the observed spectra with a Lorentzian profile with fixed width taking into account geometric and optical instrumental effects (Schneider et al. 1998). The rms noise level of the data corresponds to the average standard deviation of the fitted intensities and equals 2 × 10⁻⁵ erg s⁻¹ cm⁻² sr⁻¹ for each pixel at 158 μm and 10⁻³ erg s⁻¹ cm⁻² sr⁻¹ at 63 μm.

2.2. [C I] atomic fine structure lines and CO 7→6 and 4→3 molecular lines

The [C I] ³P₂-³P₁ and ³P₁-³P₀ lines (hereafter abbreviated by [C I] 2→1 and 1→0) and the CO 7→6 and CO 4→3 lines were mapped in 2001 October, November, and December with SMART (SubMillimeter Array Receiver for Two frequencies) at the KOSMA 3-m telescope. This 2 × 4 pixel

Table 1. Observing parameters of the molecular line data: Cols. 1 and 2 indicate the line and transition frequency, followed by the number of points observed, the observing grid and Half Power Beam Width (*HPBW*); η_{mb} is the main beam efficiency, T_{sys} the double sideband system temperature, Δv_{res} denotes the velocity resolution, and ΔT_{rms} the average rms noise temperature per channel on a T_{mb} scale.

	ν [GHz]	Points	Grid	<i>HPBW</i>	η_{mb}	T_{sys} [K]	Δv_{res} [km s ⁻¹]	ΔT_{rms} [K]
KOSMA								
¹² CO 7→6	806.651	68	55'' × 27''.5	42''	0.20	3200	0.38	1.72
¹² CO 4→3	461.041	221	27''.5	57''	0.55	1720	0.67	1.04
[C I] ³ P ₂ → ³ P ₁	809.344	68	55'' × 27''.5	42''	0.20	3200	0.38	1.72
[C I] ³ P ₁ → ³ P ₀	492.161	68	55'' × 27''.5	55''	0.50	1430	0.63	0.13
JCMT								
CN 3→2	340.248	85	6''	14''	0.68	1000	0.28	0.65
CS 7→6	342.883	85	6''	14''	0.68	1000	0.28	0.65

SIS-heterodyne receiver (Graf et al. 2002) observes simultaneously in the 490 GHz and 810 GHz atmospheric windows. The array pixels are separated by 110'' for each frequency band.

The receiver was tuned either to the [C I] 1→0 line or to the CO 4→3 line in the lower frequency channel but always to the [C I] 2→1 line in the higher frequency channel. The CO 7→6 line from the image sideband was observed simultaneously with [C I] 2→1. The receiver sideband ratio is assumed to be 1. The IF signals were analyzed with two 4-channel array-acousto-optical spectrometers with a spectral resolution of 1.5 MHz (Schieder et al. 1998). The typical double side band receiver noise temperature at 492 GHz was around 150 K and at 810 GHz between 500 and 600 K. The atmospheric transmission was derived from sky-measurements, using an atmospheric model to fit the 490 and 809 GHz bands simultaneously with a single column of perceptible water vapour and taking into account the atmospheric sideband imbalance; this procedure significantly reduces the uncertainty in the derived line ratios due the different atmospheric opacities in the two bands. The average atmospheric zenith opacity during the observations was 0.7 (1.0) for [C I] 1→0 (2→1). Observational parameters are listed in Table 1.

We employed a dual beamswitch observing mode with 6' throw. Since the PDR of S 106 is extended, we see some self-chopping effects in particular north-east and east of S 106 IR in the [C I] 1→0 line. The observed region, however, is too small to estimate the intensity subtracted out due to self-chopping. Final temperatures are on a main beam brightness temperature scale. From observations of the sun edge, we found indications for an extended errorbeam of about 200'' FWHM. Unfortunately, the map obtained in S 106 is too small to correct for the errorbeam pickup. We thus simply scale all antenna temperatures by the ratio of forward efficiency (90%) to main beam efficiency (20% at 810 GHz and 50% at 490 GHz) in order to derive the main beam temperature scale T_{mb} . The main beam efficiency was obtained from continuum scans of Jupiter. The brightness temperature of Jupiter was taken from Griffin et al. (1986) which is e.g. 174 K at 337 GHz and 144 K at 808 GHz. This method, however,

leads to an overestimate at those positions where the unknown errorbeam pickup is strong.

The pointing accuracy was estimated by cross scans on the sun and Jupiter. The relative pointing accuracy was determined to be good to within 15''. There is, however, a systematic pointing offset of around 25'' in all maps due to a misalignment of the subreflector which was corrected for.

2.3. ISO LWS observations and data reduction

ISO Long Wavelength Spectrometer Clegg et al. (1996) 44–196 μm grating scans (AOT L01) were obtained for two positions in S 106, toward S 106 IR (TDT 53000508) and toward a position 120'' in the west (TDT 74601703). The gratings contain the atomic fine structure lines [O III] 52 μm , [N III] 57 μm , [O I] 63 and 145 μm , [O III] 88 μm , and [C II] 158 μm , and the high- J CO lines ¹²CO 16→15, 15→14, and 14→13. The western spectrum was processed with the LWS Interactive Analysis (LIA, v. 8.0) and the ISO Spectral Analysis Package (ISAP, v. 2.1). In LIA, corrections were applied for dark currents, time-dependent drifts in the detector responsivities, and the absolute responsivity. In ISAP, the data were deglitched by hand, flat-fielded to the mean value of each detector using a multiplicative correction (typically less than a 1% correction, except for detector 0, where the correction was 5%), defringed (detectors 4–9), and corrected for flux clipping (the extended source correction). The detectors were then normalized (multiplicatively) to the flux level of detector 1 using the overlap regions between the detectors. Scale factors ranged from 1.01 to 1.27, which is within the 30% photometric accuracy expected between adjacent LWS detectors (LWS Handbook v. 1.2). While use of LIA improved the detector to detector matches in the western position, it degraded the matches at the central position. Therefore, only the ISAP reduction steps were performed. Additionally, detectors 0, 1, 6, and 7 suffered memory effects at S 106 IR, so only one scan direction was used for portions of these data.

Table 2. ISO LWS flux densities, surface brightnesses, and beam sizes (from Table 4.9 in the ISO-LWS handbook v. 1.2) for the observed FIR lines in S 106 IR and S 106 West. *The [O I] 63 μm , [O III] 88 μm , and [O I] 145 μm lines were each present in two detectors so that we calculated the error from the weighted mean for the flux and brightness. The errors given in the Table reflect the uncertainty from the line fitting process, not the 30% absolute photometry uncertainty for LWS.

	λ [μm]	LWS Flux density [$10^{-2} \text{ erg s}^{-1} \text{ cm}^{-2} \mu\text{m}^{-1} \text{ sr}^{-1}$]	LWS Brightness [$10^{-3} \text{ erg s}^{-1} \text{ cm}^{-2} \text{ sr}^{-1}$]	KAO Brightness	LWS beam [10^{-7} sr]	KAO beam [10^{-7} sr]
S 106 IR						
[O III]	51.815	0.94 ± 0.05	2.90 ± 0.15		1.24	
[N III]	57.330	0.24 ± 0.04	0.75 ± 0.12		1.24	
[O I]*	63.184	2.185 ± 0.04	6.39 ± 0.07	21	1.24	0.13
[O III]*	88.356	0.175 ± 0.01	0.72 ± 0.03		1.18	
[O I]*	145.525	0.115 ± 0.01	0.74 ± 0.03		0.90	
[C II]	157.741	0.17 ± 0.01	1.07 ± 0.03	0.8	0.85	0.86
CO 16 \rightarrow 15	162.812	0.0045 ± 0.002	0.024 ± 0.001		0.85	
CO 15 \rightarrow 14	173.631	0.009 ± 0.003	0.059 ± 0.020		0.80	
CO 14 \rightarrow 13	185.999	0.009 ± 0.002	0.055 ± 0.015		0.80	
S 106 West						
[O III]	51.815	0.026 ± 0.002	0.081 ± 0.007		1.24	
[O I]*	63.184	0.123 ± 0.002	0.36 ± 0.002		1.24	
[O III]*	88.356	0.0285 ± 0.002	0.12 ± 0.008		1.18	
[O I]*	145.525	0.007 ± 0.002	0.045 ± 0.001		0.90	
[C II]	157.741	0.096 ± 0.001	0.61 ± 0.008	0.2	0.80	0.86

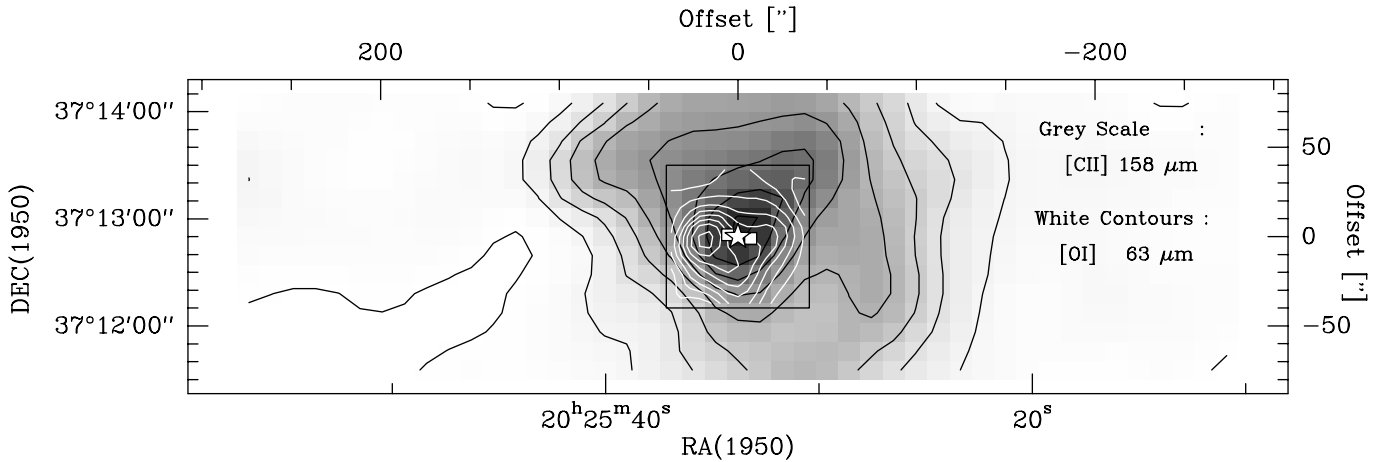


Fig. 1. The [C II] emission distribution as grey scale (with contour levels from $(0.5 \text{ to } 8.5 \text{ by } 1) \times 10^{-4} \text{ erg sr}^{-1} \text{ s}^{-1} \text{ cm}^{-2}$) shows a pronounced peak close to the position of the exciting star S 106 IR (marked by a star symbol). The two squares denote the locations of peak dust continuum emission at 1.3 mm (Mezger et al. 1987) and at 450 μm and 800 μm (Richer et al. 1993). The western peak is referred to as S 106 FIR. Overlaid as white contours is the [O I] 63 μm map (the square box indicates the mapped region) with contour levels from $(2.3 \text{ to } 20.7 \text{ by } 2.3) \times 10^{-3} \text{ erg sr}^{-1} \text{ s}^{-1} \text{ cm}^{-2}$ increasing from outside to inside.

Line strengths were measured within ISAP after first converting intensity to brightness. Because the lines are unresolved, the line widths were held to the instrumental line width: 0.29 or 0.60 μm for detectors 0–4 and 5–9, respectively.

Comparing the LWS spectra to the data obtained with the KAO (Col. 5 in Table 2) we find (i) that the ISO [C II] intensity is a factor of 1.3 (3) larger than the findings for the positions of S 106 IR (S 106 W) using the KAO and (ii) that the [O I] intensity towards S 106 IR is a factor of 3 weaker than the

KAO value. The difference for [O I] can be explained by beam dilution: the KAO [O I] map (Fig. 1), covering approximately the beam area of the ISO spectrum, shows that the emission is not homogeneous and decreases rapidly at the borders. When we recalculate the KAO [O I] intensity in the ISO beam, considering a Gaussian intensity distribution, we arrive at a value of $0.7 \times 10^{-2} \text{ erg s}^{-1} \text{ cm}^{-2} \text{ sr}^{-1}$, very close to the intensity observed with ISO.

The three times stronger [C II] emission at position S 106 W in the ISO beam might be due to the different observing modes: The KAO observations were performed using a dual beamswitch of several arcminutes in N-S direction while the ISO spectra were taken without a reference position. Therefore the ISO data might at least partly be contaminated by extended emission and/or unrelated emission features in the foreground/background.

The ISO CO 14→13 line brightness at the position of S 106 IR is a factor of 2 smaller than the observed *upper limit* value of $0.13 \times 10^{-3} \text{ erg s}^{-1} \text{ cm}^{-2} \text{ sr}^{-1}$ obtained by Graf et al. (1993) with the KAO at the same angular resolution (the line intensity uncertainty is, however, 30%).

2.4. CN 3→2 and CS 7→6 molecular lines

The CN and CS submillimeter observations were obtained at the James Clerk Maxwell Telescope (JCMT)¹ on Mauna Kea, Hawaii, during one shift in 1995 June. The hyperfine structure pattern of CN $N = 3 \rightarrow 2$ (340.248 GHz for the strongest component) was observed simultaneously with the CS $J = 7 \rightarrow 6$ transition from the image sideband with the B3i SIS receiver. This procedure guarantees identical pointing between the two line maps. The spectra were obtained in an OTF mapping technique. A total of 85 spectra in each transition was obtained with a resulting grid spacing of $6''$ and an integration time on each source position of 10 s. The spectra were calibrated for atmospheric attenuation with a standard chopper wheel method. We used the 500 MHz wide standard configuration of the autocorrelator, providing a channel spacing of 313 kHz. A receiver sideband ratio of unity was assumed. The line intensities are given on a T_{mb} scale (using a value of $\eta_{\text{mb}} = 0.68$ at 340 GHz, as determined from observations of Jupiter and Mars). Pointing was checked regularly and found to be better than $5''$.

3. Results

3.1. Atomic fine structure maps

3.1.1. [C II] 158 μm line emission

The [C II] line traces warm, moderately dense gas since the critical density n_{cr} is $3 \times 10^3 \text{ cm}^{-3}$ and $5 \times 10^3 \text{ cm}^{-3}$ for collisions with atomic and molecular hydrogen, respectively (Tielens & Hollenbach 1985; Genzel et al. 1989) at temperatures higher than 90 K. In the classical picture of the sequential structure of a PDR with high gas density ($10^3 \text{ cm}^{-3} < n < 10^6 \text{ cm}^{-3}$) irradiated by high FUV fluxes ($10^3 < G_0 < 10^6$) (Tielens & Hollenbach 1985), the atomic lines of [C II], [O I] and H trace the outermost layer at a visual extinction of $A_v \approx 1^m$, followed by the transition region of atomic to molecular hydrogen ($A_v \sim 1-2^m$). At $A_v \sim 2-5^m$, a cooler ($T \sim 50 \text{ K}$), partly dissociated layer is dominated by [C I] emission while the even cooler interior of the PDR ($A_v \sim 10^m$) is predominantly emitting in

CO rotational lines. This scenario slightly changes if lower density and FUV intensity PDRs are considered (Hollenbach et al. 1991): a surface layer of $A_v \leq 1-2^m$ consists of H, O, and C^+ with a transition to H_2 and to C at $A_v \geq 1-2^m$. Carbon (oxygen) is in the form of CO at $A_v \geq 4-6^m$ ($A_v \sim 10^m$).

Our [C II] 158 μm map, displayed as a grey scale image in Fig. 1 together with the [O I] 63 μm emission as white contours, covers an area of $10' \times 3'$ ($1.75 \times 0.5 \text{ pc}$ at a distance of 600 pc) centered on S 106 IR. The [C II] line was detected well above the 3σ -level at 60 positions out of the observed 75. The location of peak [C II] emission is found in the immediate environment around S 106 IR on a size scale of $4' \times 3'$. The [C II] emission is north-east to south-west oriented with strong emission gradients east and west of S 106 IR. The overall distribution is rather smooth and similar to the CO 7→6 emission (Fig. 5) observed with KOSMA, and the higher angular resolution (15 points at $25''$) CO 7→6 map published by Harris et al. (1987). The peak [C II] intensity of $8 \times 10^{-4} \text{ erg s}^{-1} \text{ cm}^{-2} \text{ sr}^{-1}$, found at the position of S 106 IR, is about thirty times the noise level for one pixel.

3.1.2. [O I] 63 μm emission

The [O I] 63 μm observations, on top of the [C II] data in Fig. 1, show more structure than the [C II] map due to the higher angular resolution ($22''$). The [O I] line traces denser ($n_{\text{cr}} = 5 \times 10^5 \text{ cm}^{-3}$ and $7 \times 10^5 \text{ cm}^{-3}$ for collisions with atomic and molecular hydrogen, respectively Tielens & Hollenbach 1985; Genzel et al. 1989), higher excited ($T \approx 200 \text{ K}$) gas and is much brighter than the [C II] 158 μm line, even if we smooth the $22''$ resolution [O I] emission to the $55''$ resolution of the [C II] line. The peak intensity in a $22''$ beam is $2.1 \times 10^{-2} \text{ erg s}^{-1} \text{ cm}^{-2} \text{ sr}^{-1}$ at a position ($20'', 0$) offset from S 106 IR, which is a factor of 26 stronger than the [C II] intensity.

The [O I] emission extends to the south of S 106 IR, marking a presumably edge-on PDR region, which was resolved in high angular resolution Br α and 3.29 μm PAH observations by Smith et al. (2001). The eastern region of more intense [O I] emission is correlated with the so-called “East clump” (Little et al. 1995), which they interpret as the remnant of a molecular toroid around S 106 IR, and the (sub)mm-continuum peak found by Mezger et al. (1987) and Richer et al. (1993). The contour lines of [O I] emission about $20''$ west of S 106 IR indicate a beam diluted secondary peak correlated with S 106 FIR (Richer et al. 1993) which was also seen in the 60 μm continuum observations of Cole (1997) and in H_2O maser emission (Stutzki et al. 1982). The maser emission was recently resolved into two clusters of H_2O maser spots with 50 AU separation in 22 GHz VLA and VLBA observations by Furuya et al. (1999).

Due to the correlation with maser emission, Richer et al. (1993) and Furuya et al. (1999) interpret S 106 FIR as a self-luminous protostellar object. In contrast, Little et al. (1995) attribute their observations of the [C I] 609 μm emission to the existence of an externally illuminated (by S 106 IR) PDR without the necessity of an internal source.

¹ The JCMT is operated by The Observatories on behalf of the Particle Physics and Astronomy Research Council of the United Kingdom, the Netherlands Organisation for Scientific Research, and the National Research Council of Canada.

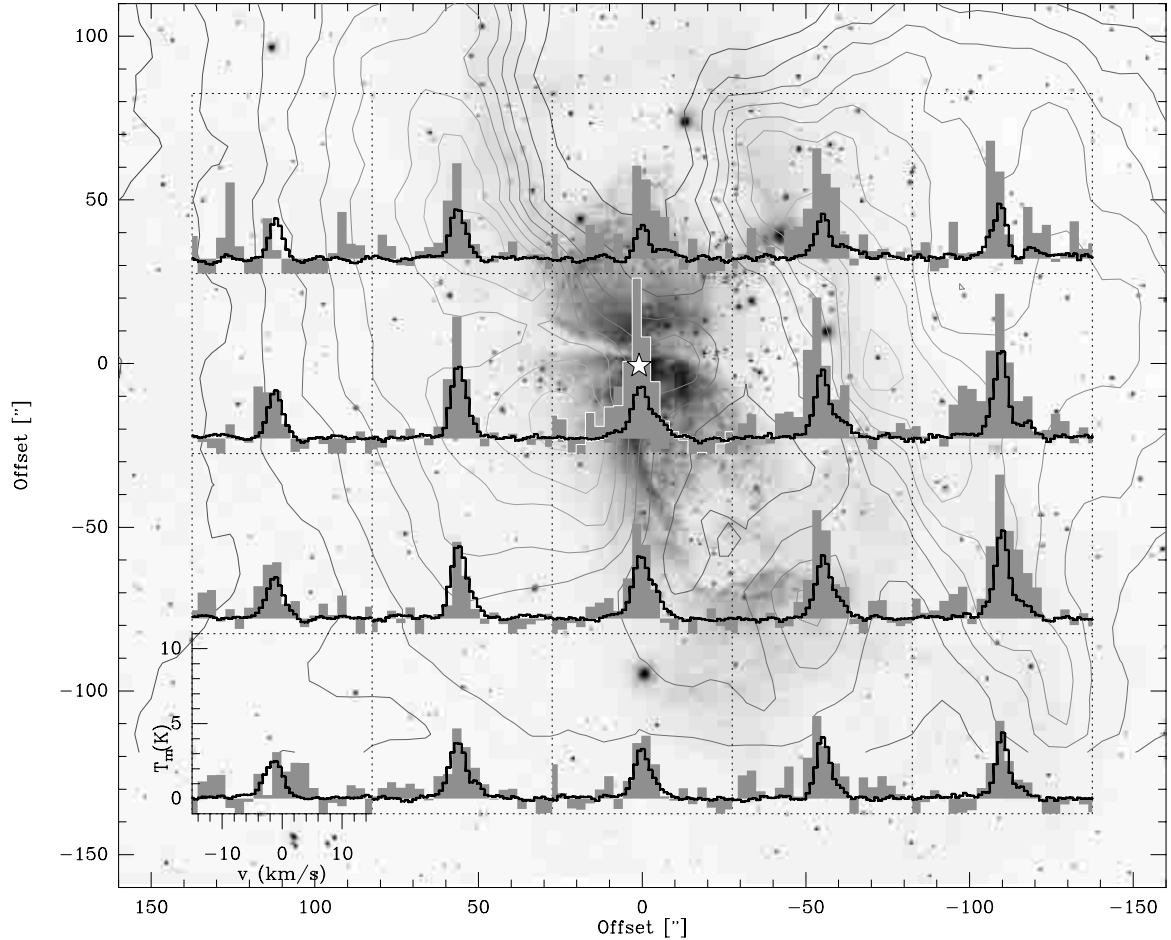


Fig. 2. Spectra of [C I] 2→1 (grey shaded, spectra are smoothed to 1.6 km s^{-1} resolution) and [C I] 1→0 (black line) emission, overlaid on an IR image of Subaru (each spectrum is centered on the appropriate position, e.g., the lower left box shows the spectrum taken towards the position $110'', -110''$). The grey contours (levels 0.85 to 13.6 by 0.85 K km s^{-1}) represent the -1.3 km s^{-1} velocity plane of ^{13}CO 2→1 emission obtained with IRAM (Schneider et al. 2002).

3.1.3. [C I] 2→1 and 1→0 emission

The [C I] 1→0 line has an upper level energy above ground of 24 K and a critical density of 10^4 (4.7×10^2) cm^{-3} for collisions with H_2 (H), which makes it easy to excite this level. Significant abundances of neutral carbon in chemical models, however, are only predicted in a thin layer ($A_v < 3^m$) of PDRs between regions of ionized carbon and molecular CO. All [C I] observations so far show extended emission well correlated with low- J CO (see Plume et al. 1999 for an overview). The line brightness temperatures are typically a few Kelvin.

Our [C I] 1→0 observations fit very well into this scenario. A selection of spectra are displayed in Fig. 2 together with the [C I] 2→1 line, both placed on their respective position on an IR image of S 106 taken with Subaru². Grey contour lines indicate the bulk emission of the molecular cloud, i.e., the -1.3 km s^{-1} velocity plane of ^{13}CO 2→1 emission observed with IRAM (Schneider et al. 2002). The [C I] 1→0

main beam brightness temperature ranges between ≈ 2 and 6 K (maximum at $-110'', 0$) and shows a rather homogeneous intensity distribution without strong temperature gradients. The main line component has a velocity of around -1.2 km s^{-1} but several spectra have non-gaussian line profiles with broad red- and/or blueshifted wing emission. The red wing is best visible at all positions with RA-Offset between 0 and $-55''$. Around $(-110'', 0)$ an additional line component around $+2 \text{ km s}^{-1}$ is evident. The blue wing is seen at $(0, 0)$ and $(0, -55'')$. The broad line wings in the immediate environment of S 106 IR, particularly blueshifted emission in a dense clump east of S 106 IR, were previously detected in observations of isotopomeric CO lines (Schneider et al. 2002). The broad wing emission is attributed to the impact of the stellar wind of S 106 IR on the molecular gas and the dip in the line profile around 2 km s^{-1} is due to self-absorption effects (and not to a separate velocity component). We conclude that this is also true for the blue and redshifted high-velocity emission seen in the [C I] 1→0 line.

The [C I] 2→1 line is also easy to excite (the energy above ground level is 62.5 K and $n_{\text{cr}} = 10^4 \text{ cm}^{-3}$ considering collisions with both H or H_2). The spectra are shown in Fig. 2. The

² Subaru is an 8.2 meter optical-infrared telescope at the summit of Mauna Kea, Hawaii, operated by the National Astronomical Observatory of Japan (NAOJ) with the support of the Ministry of Education, Culture, Sports, Science, and Technology.

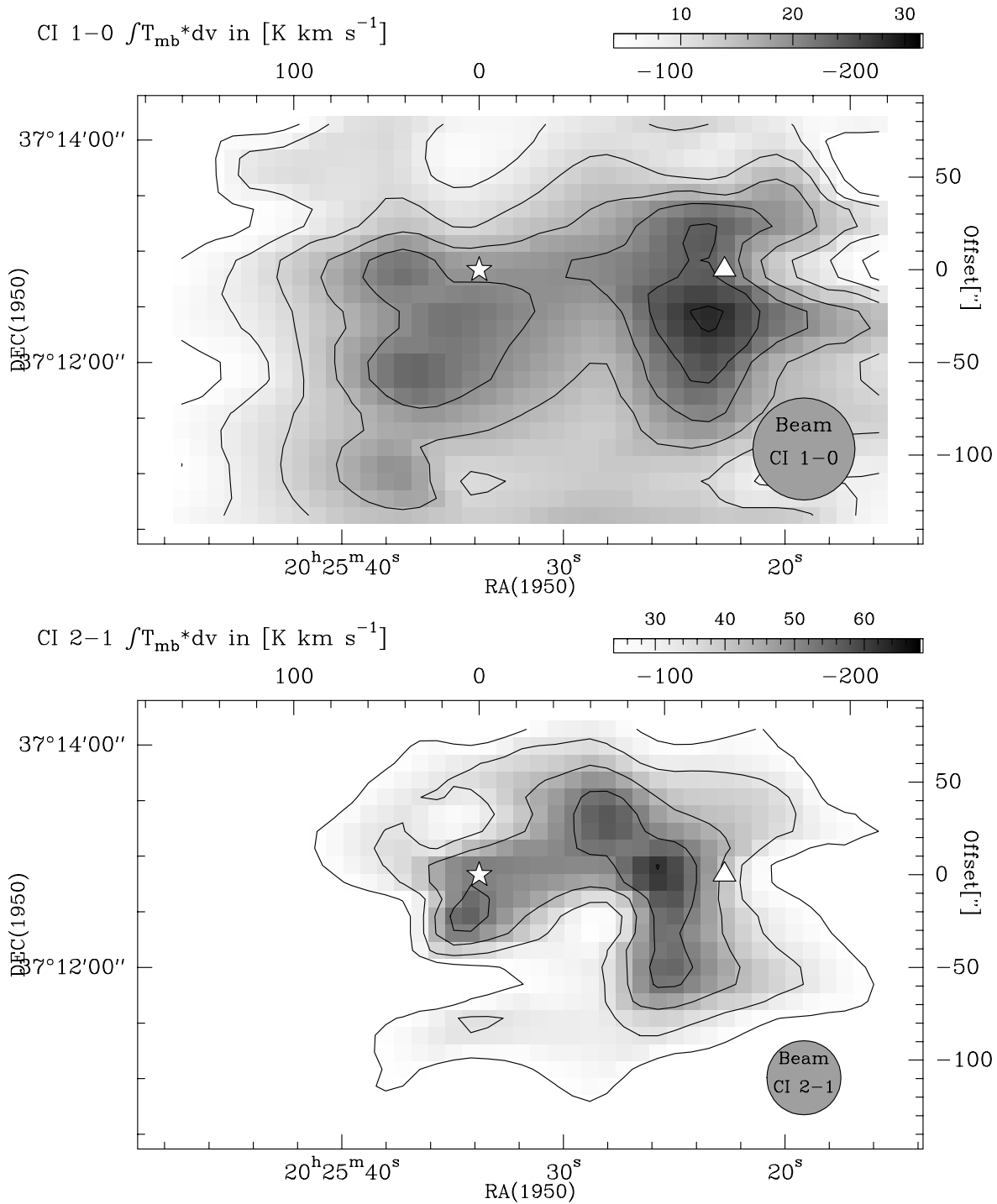


Fig. 3. Maps of the line integrated [C I] 1→0 (top) and 2→1 (bottom) emission in the velocity range -7 to 7 km s^{-1} . The contour ranges are as follows (in the notation start/end/step): [C I] 1→0: $4/28/4$ K km s^{-1} ($3\sigma = 3.6$ K km s^{-1}), [C I] 2→1: $24/62/9.5$ K km s^{-1} ($3\sigma = 12$ K km s^{-1}). S 106 IR is marked by a star, the triangle indicates the position close to the NH_3 emission peak where an ISO LWS scan was taken.

main beam brightness temperatures vary between 2 and 10 K. The absolute intensities, however, have to be treated with caution since they may be too high due to errorbeam pickup. All line temperatures at the center and in the north-western part of the map are a factor of 1.5 to 2 higher than the [C I] 1→0 values, in contrast to the south-east, where the line profiles and temperatures are very similar. Broad wing emission in the [C I] 2→1 line is more difficult to identify due to the higher

noise in the spectra compared to [C I] 1→0. At all positions close to $(-110'', -110'')$, however, the red wing can be clearly seen and blue wing emission is strong towards S 106 IR $(0,0)$ and at positions $(-55'', 0)$, $(-55'', 55'')$, and $(-110'', 0)$.

Velocity integrated ($v = -7$ to 7 km s^{-1}) maps of [C I] 2→1 and 1→0 emission are presented in Fig. 3. The [C I] 1→0 map (top) shows a double peak structure with a maximum close to the position of peak emission of NH_3 (Stutzki et al. 1982, close

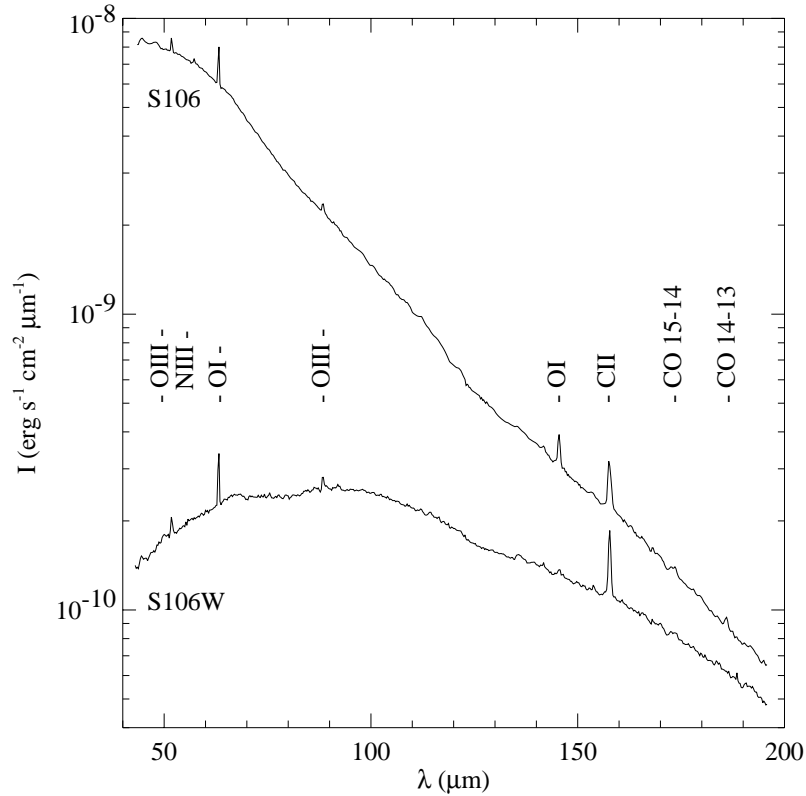


Fig. 4. ISO LWS grating for S 106 IR (top line) and S 106 West (bottom line). The high- J CO lines and FIR PDR tracing lines are marked.

to the triangle, which marks the observed ISO position in the west ($-120''$, 0) and hereafter is called S 106 W) and a weaker peak south of S 106 IR. The map shows some striping effects in east-west direction because it was observed fully-sampled in Declination but only beam-sampled in RA. In addition, self-chopping effects may have filtered out some emission east and north-east of S 106 IR. Both peak emission regions are evident in the [C I] $2 \rightarrow 1$ map, but the western peak region is shifted towards S 106 IR. This peak is linked to the more distinct eastern peak via a low intensity bridge of emission.

3.2. ISO atomic fine structure data

The ISO LWS grating scans taken at S 106 IR and S 106 W are shown together in Fig. 4. The detected FIR fine-structure and high- J CO lines are marked in the plot, the respective fluxes and brightnesses are given in Table 2. Towards S 106 IR, the underlying continuum is much stronger than for S 106 W and more lines are detected (e.g., the [O I] $145 \mu\text{m}$ line or the high- J CO lines, which are not seen at all at S 106 W). In addition, the intensity ratios for the same line at the two positions vary between 1.8 (for the [O I] $63 \mu\text{m}$ and [C II] $158 \mu\text{m}$ lines) and 16 (36) for [O I] $145 \mu\text{m}$ ([O I] $52 \mu\text{m}$). This implies higher densities and a stronger UV field at S 106 IR, favouring the excitation of PDR tracing lines, in particular those of [O I], which have higher critical densities. The position of S 106 IR was also observed with the LWS by van den Ancker et al. (2000) who obtained similar values for the atomic fine structure lines.

3.3. Molecular line maps

3.3.1. CO $7 \rightarrow 6$ and CO $4 \rightarrow 3$ emission

The CO $4 \rightarrow 3$ transition is a tracer of warm ($T \sim 50$ K) and dense ($n_{\text{cr}} \sim 10^5 \text{ cm}^{-3}$) molecular gas. The CO $7 \rightarrow 6$ line requires even higher densities and temperatures ($T \sim 150$ K, $n_{\text{cr}} \sim 10^6 \text{ cm}^{-3}$) for thermalization. The CO $4 \rightarrow 3$ emission distribution, shown in Fig. 5 (top), is characterized by one prominent, beam diluted peak at the position of S 106 IR embedded in extended emission with a weaker secondary peak south of the NH_3 peak in the western part of the cloud at $\approx -120''$, $-70''$. The emission features further west are partly due to bad S/N spectra.

The CO $7 \rightarrow 6$ emission distribution (Fig. 5, bottom) is very similar to that of CO $4 \rightarrow 3$, but shows a slightly more pronounced elongated east-west morphology due to the different sampling only (the CO $4 \rightarrow 3$ map is fully sampled in RA and DEC), and some extended emission maybe partly due to errorbeam pickup. The CO $7 \rightarrow 6$ peak is connected to the NH_3 peak by a bridge of lower intensity emission. The $25''$ angular resolution CO $7 \rightarrow 6$ map obtained by Harris et al. (1987) shows the same emission distribution from a beam diluted compact source centered on S 106 IR. They observed a peak main beam brightness temperature of 39–61 K. Our value of 33 K in a $\sim 40''$ beam is therefore consistent with the Harris et al. (1987) observations considering the different beam sizes.

We selected 8 spectra (Fig. 6) in the CO $7 \rightarrow 6$ line in order to illustrate the dynamics of the region. As in Fig. 2, the spectra are overlaid on an IR image of S 106 including

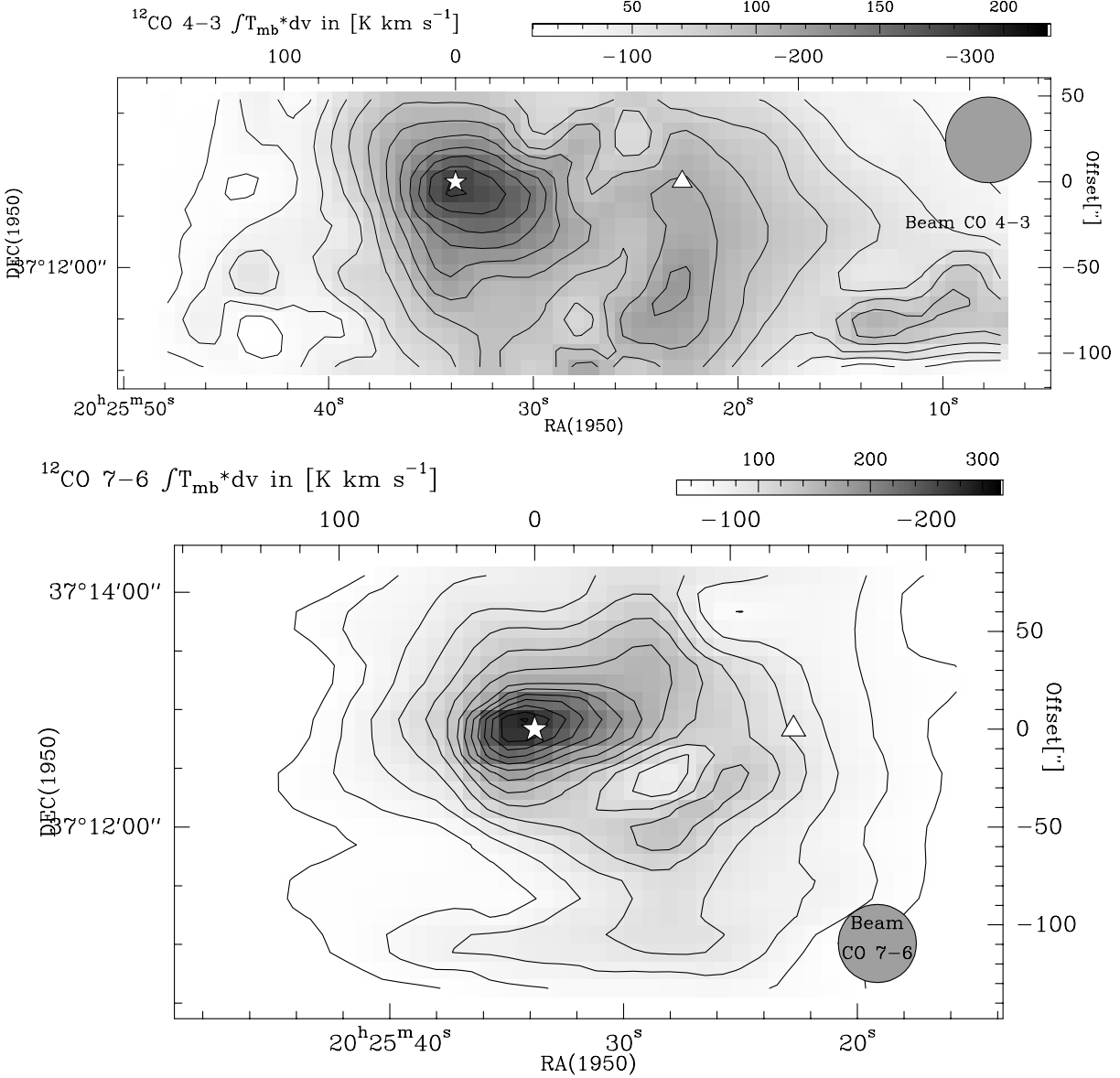


Fig. 5. Maps of the line integrated CO 4→3 (top) and CO 7→6 (bottom) emission in the velocity range -7 to 7 km s^{-1} . The contour ranges are as follows (in the notation start/end/step): CO 4→3: 15/180/15 K km s^{-1} ($3\sigma = 12$ K km s^{-1}), CO 7→6: 27/287/20 K km s^{-1} ($3\sigma = 13.5$ K km s^{-1}). S 106 IR is marked by a star, the triangle indicates the position close to the NH_3 emission peak where an ISO LWS scan was taken.

contour lines of ^{13}CO 2→1 emission. For this plot, we chose the 2.5 km s^{-1} velocity plane in order to emphasize the distribution of redshifted high-velocity emission. Most of the spectra show broad blue and/or red wing emission in the velocity range from -10 to 6 km s^{-1} with typical linewidths of 8 – 9 km s^{-1} . The wings are most apparent at S 106 IR (0,0) but also prominent at offsets $(-55'', 0)$ and $(-55'', 55'')$. These spectra towards the west are located in a highly dynamic region where the H II region interfaces the molecular cloud and the stellar wind from S 106 IR hits the molecular cloud edges, driving a shock into the cloud. The 2.5 km s^{-1} CO contour lines mark the region where molecular gas is swept-up by the stellar wind in the foreground (Schneider et al. 2002). Spectra towards the remaining positions have more Gaussian shapes and typical line widths of 3 – 4 km s^{-1} . This differs from observations of the CO 7→6 line in very luminous sources (W 49, W 51) by Jaffe et al. (1987), who found bright (T_{mb} typically 50 K) and broad

($\Delta v \sim 10$ – 24 km s^{-1}) lines. In our case, the CO 7→6 spectra are more similar to the low- J CO data, also reflecting the dynamics due to the interaction of the high velocity stellar wind from S 106 IR with the molecular gas, but indicating a smaller amount of hot gas.

3.3.2. CN $N=3\rightarrow 2$ and CS $J=7\rightarrow 6$ emission

Figure 7 shows line integrated maps of CS $J=7\rightarrow 6$ and CN $N=3\rightarrow 2$, taken at $14''$ angular resolution with the JCMT, together with overlays of the same maps to the $[\text{O I}]$ emission. Both molecular lines have similar high critical densities (3×10^7 cm^{-3} for CS 7→6 and 9×10^6 cm^{-3} for CN $N=3\rightarrow 2$) but different energies of the upper rotational level above the ground state: 66 K for CS and 33 K for CN. Differences in the emission distribution of the two transitions will consequently trace either

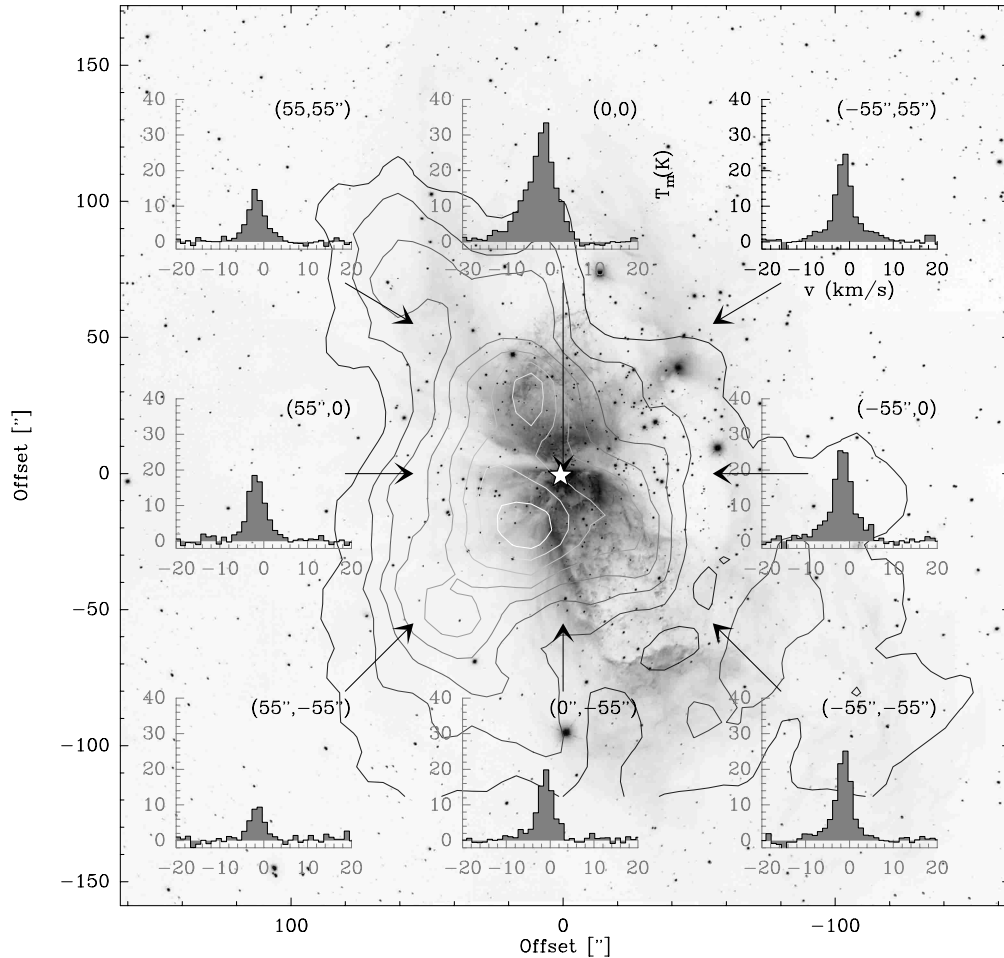


Fig. 6. Spectra of ^{12}CO 7 \rightarrow 6 emission (smoothed to a velocity resolution of 1.2 km s^{-1}) plotted on an IR picture of S 106 made with Subaru. The grey contours (levels 1 to 7 by 1 K km s^{-1}) represent the 2.5 km s^{-1} velocity plane of ^{13}CO 2 \rightarrow 1 emission obtained with IRAM (Schneider et al. 2002).

different temperatures or abundance variations. CS marks very well the warm and dense inner part of the East clump, slightly shifted towards S 106 IR. A bridge of emission extends to the west towards S 106 FIR and forms a second, weaker maximum. In contrast, the CN map shows two equally strong maxima at the position of the East clump, slightly shifted to the east with respect to the CS peak, and S 106 FIR.

Channel maps of CN and CS, not shown here, further reveal the morphological differences in the emission. At low velocities, around -2 km s^{-1} , CN emission is elongated in east-west direction and follows the dark lane seen at optical wavelengths and in the IR image (e.g., Fig. 2) while CS 7 \rightarrow 6 is concentrated just east of S 106 IR. The emission pattern for CS 7 \rightarrow 6 and CN 3 \rightarrow 2 at these velocities is thus very similar to that of ^{12}CO and ^{13}CO 2 \rightarrow 1, respectively (see the CO channel maps in Schneider et al. 2002). At velocities $> -2 \text{ km s}^{-1}$, associated with the bulk emission of the cloud at -1.3 km s^{-1} , both CN and CS start to trace S 106 FIR. The emission peaks associated with the East clump are still shifted in the sense that the CS peak is closer to S 106 IR. In addition, CN emission is again much more east-west elongated compared to that of CS, which is more confined to the vicinities of S 106 IR and FIR. The observed shift between the emission peaks cannot be attributed

to pointing uncertainties since both transitions were observed simultaneously with the same receiver. It is also not due to abundance variations in the PDR gas, which would result in exactly the opposite behavior. Model calculations by Sternberg & Dalgarno (1989) and Jansen et al. (1996) show that CN is more abundant in zones closer to the PDR surface where the UV field is only partly attenuated, whereas CS becomes abundant at larger (and more shielded) depths closer to the core of the clump. Such a chemical stratification has already been observed in, e.g., the Orion Bar region (Simon et al. 1997 for the CN and CS transitions discussed here). Using the PDR model of Sternberg & Dalgarno (1989), at a distance of 600 pc, a density of the East clump of 10^5 cm^{-3} and an incident UV field of $10^3 G_0$ (see Fig. 13), the CN peak facing S 106 IR and the CS peak towards the East clump would be displaced by only a few arcsec, well below the angular resolution of $14''$. Based on the fact that both transitions have similar critical densities but different energies above ground, the observed difference in the CN and CS distribution is probably due to CS tracing the warmer part of the East clump facing S 106 IR.

The situation is different towards S 106 FIR, where CN 3 \rightarrow 2 peak emission between -1 and 0 km s^{-1} is more pronounced than that of CS 7 \rightarrow 6. Previous observations led to the

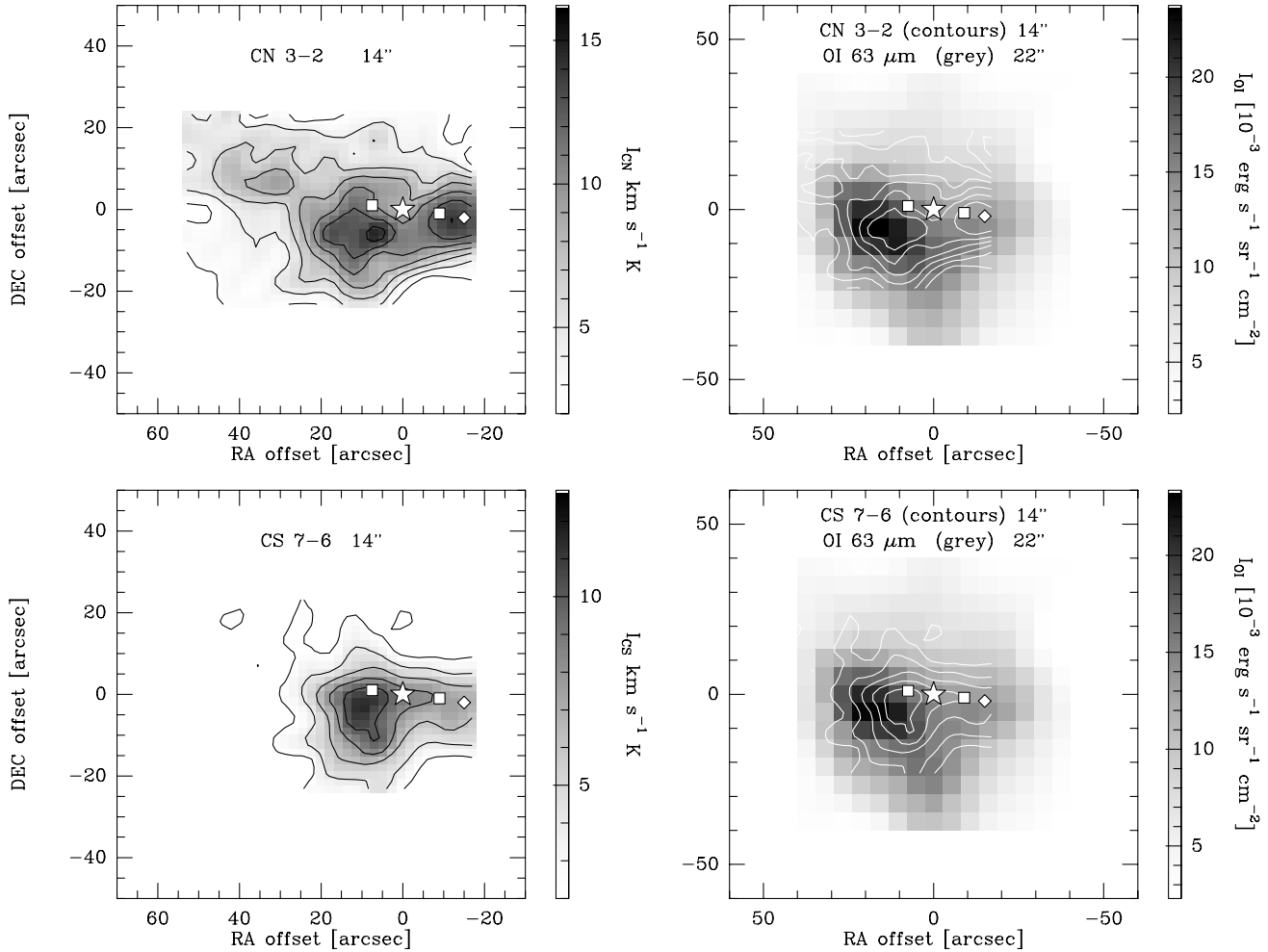


Fig. 7. *Left top and bottom:* grey scale maps of the line integrated CN 3→2 and CS 7→6 emission both at 14'' angular resolution. *Right top and bottom:* the same molecular line maps as contours, overlaid on the [O I] 63 μm emission at 22'' resolution as a grey scale. Both lines are integrated over a velocity range of -7 to 1 km s $^{-1}$. Contours start at the 3σ -level of 1.95 K km s $^{-1}$ and increase in steps of 3σ . The position of S 106 IR is marked by a star, the Mezger et al. (1987) submm peaks by squares and the source S 106 FIR as a rhombus.

conclusion that S 106 FIR is associated with warm and dense ($\sim 10^5$ cm $^{-3}$) gas (Richer et al. 1993; Little et al. 1995). The observed brighter CN emission compared to CS then is readily explained if there is a higher degree of clumpiness in the part of the cloud west of S 106 IR. The CN abundance is thus enhanced on the clump surfaces throughout this region. The [O I] emission (Fig. 1), as a high density and PDR tracer, fits perfectly in this scenario: it outlines the dense East clump and shows a second, weaker emission peak at S 106 FIR.

3.4. Intercomparison of PDR tracer lines

In Figs. 8 and 9 we display overlays of the [C I] 1→0 and CO 7→6 emission as grey scales with emission contours of other lines ([C II], [C I] 2→1, ^{12}CO and ^{13}CO 2→1). In Fig. 8, we see a good morphological correlation between [C I] and ^{13}CO 2→1 emission (CO data taken from Schneider et al. 2002), as it was already found for other Galactic PDR regions (e.g., Plume et al. 1999). Prominent is the strong emission from the “East clump” (at offset 20'', 0), which is partly beam diluted in [C I] emission and maybe affected by self-chopping effects.

Even on a larger scale, the [C I] and CO emission correlation is good: Both lobes of emission west and east of S 106 IR are nicely outlined by similar contours of both tracers. The intensity of the emission peaks for the lines are reversed: the eastern peak is more pronounced in CO, while the western lobe harbors the stronger [C I] peak. Since both lines are optically thin ($\tau(^{13}\text{CO } 2 \rightarrow 1) < 1$, see Table 2 in Schneider et al. 2002; and $\tau([\text{C I}] 1 \rightarrow 0) \simeq 0.1$, see Table 4 in this paper), this indicates that there are abundance differences between the two regions. A plausible explanation would be that the gas is less dense/more clumpy, and thus more tenuous, towards the west, allowing UV radiation to penetrate deeper into the cloud and therefore favouring the creation of PDRs with [C I] emission.

Figure 9 displays the CO 7→6 emission as a grey scale and ^{12}CO 2→1 (a), [C II] (b), and [C I] 2→1 (c) emission overlaid as white/dashed contours. Generally, the emission distributions of the CO 7→6 and all other lines are very similar in that they show a prominent, beam diluted peak at the position of S 106 IR. In particular the CO 7→6 and [C II] lines mark the hottest part of the PDR, which extends from S 106 IR northwards and then further to the west, building a bridge of

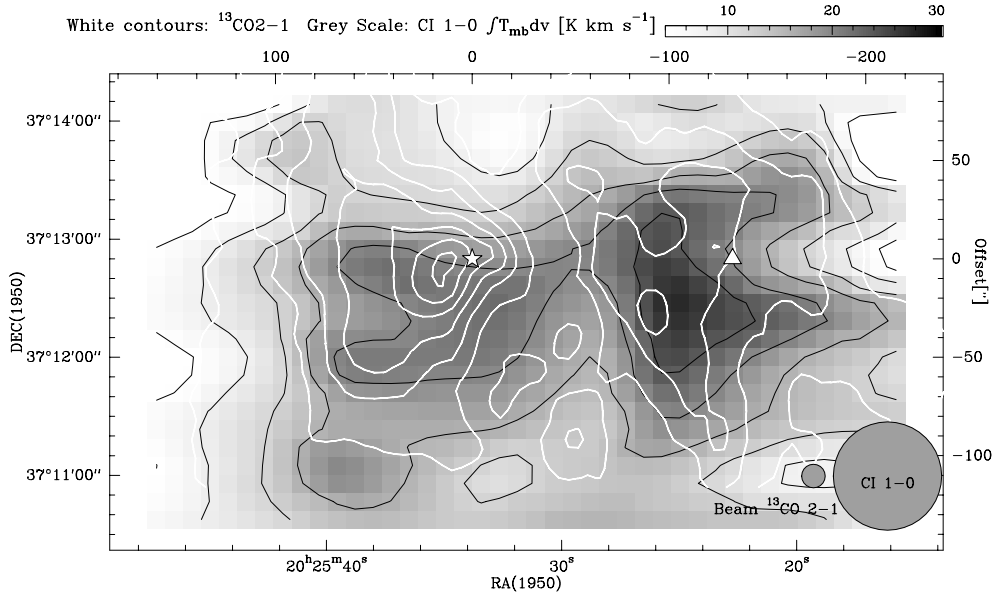


Fig. 8. Maps of the line integrated [C I] 1→0 emission (as a grey scale) overlaid with ^{13}CO 2→1 emission as white contours. The position of S 106 IR is marked by a star and the ISO LWS position as a triangle. The contour ranges are (in the notation start/end/step): ^{13}CO 2→1 40/160/20 K km s^{-1} ($3\sigma = 23.5 \text{ K km s}^{-1}$), and [C I] 1→0 4/28/4 K km s^{-1} ($3\sigma = 3.6 \text{ K km s}^{-1}$).

emission to the NH_3 peak. The similar contours for the maps of ionized and neutral carbon, and CO 7→6 argue for the co-existence of the three tracers. The line opacities, however, may differ significantly from very low (0.1) for [C I] (see Table 4) to close to 1 for [C II] and probably also for CO 7→6, but we can not judge this from our observations. The ^{12}CO 2→1 emission, tracing cooler molecular gas, is much more extended towards the east, almost avoiding the northwestern emission bridge. Its optical depth is presumably high since it is a low- J CO line.

4. Analysis

4.1. The [C II] to FIR flux ratio

The total flux of the [C II] line summing over the central array pixels around S 106 IR is $5.85 \times 10^{-3} \text{ erg cm}^{-2} \text{ s}^{-1}$. This is equivalent to a total luminosity of $48 L_{\odot}$ considering a distance of 600 pc. The bolometric FIR flux at 50 and 100 μm was determined by Harvey et al. (1982) from airborne observations. They obtained a flux density of $F_{50} = 1.7 \times 10^4 \text{ Jy}$ (44–59 μm) and $F_{100} = 1.4 \times 10^4 \text{ Jy}$ (75–155 μm) with an accuracy of $\pm 30\%$ in a $3/5$ diameter region centered on S 106 IR. From the ISO observations in Fig. 4 we see that the spectral energy distribution between 50 and 155 μm away from S 106 IR is rather flat, so that we simply integrate $\Delta\nu (F_{50} + F_{100})/2$ to derive a total flux of $6.3 \times 10^{-7} \text{ erg s}^{-1} \text{ cm}^{-2}$ or $7100 L_{\odot}$.

We then obtain an upper limit to the flux ratio $F_{[\text{C II}]} / F_{\text{FIR}}$ of 6.75×10^{-3} or 0.7%, which is slightly higher than the values ($1\text{--}3 \times 10^{-3}$) found by (Stacey et al. 1991a) for other Galactic star forming regions. It agrees well with the ratio of 10×10^{-3} for the Rosette molecular cloud (Schneider et al. 1998) and NGC 1977 (Howe et al. 1991).

4.2. Excitation conditions from high- J CO lines

At the position of S 106 IR, we determined a CO 16→15/CO 14→13 line ratio of 0.44 from ISO (see Table 2) and used the CO 7→6 intensity observed with KOSMA to obtain the kinetic temperature, H_2 -density, and CO column density from a non-LTE escape probability model (Stutzki & Winnewisser 1985). Although the beam filling factor η_b of the CO 7→6 line is unknown, we can set a lower limit of 200 K for the temperature at a minimum density of $5 \times 10^6 \text{ cm}^{-3}$ and total CO column density divided by the line width ($N_{\text{CO}}/\Delta\nu$) of $6 \times 10^{15} \text{ cm}^{-2}/(\text{km s}^{-1})$. The quantities from the observed lines are not compatible with lower temperatures. For higher temperatures, the model densities decrease gradually with increasing temperature (10^6 , 5×10^5 , and $3 \times 10^5 \text{ cm}^{-3}$ for 300, 400, and 500 K) at constant column density. The beam filling mainly affects the column density and leads to significantly higher values in case of $\eta_b \ll 1$. For example, $\eta_b = 0.1$ gives $N_{\text{CO}}/\Delta\nu \sim 6 \times 10^{17} \text{ cm}^{-2}/(\text{km s}^{-1})$ at 300 K, a value which was found by Harris et al. (1987) for temperatures between 200 and 500 K. From an H_2 excitation diagram, using pure rotational transitions of H_2 observed with ISO, and assuming optically thin emission, van den Ancker et al. (2000) derived an excitation temperature of 420 K. A similar temperature of 490 K was found from a CO excitation diagram, using high- J CO lines observed with ISO and equally assuming optically thin emission (van den Ancker et al. 2000) confirming the earlier estimate of 200–500 K, derived from the analysis of the CO 7→6 and 14→13 lines by Harris et al. (1987).

4.3. The ratio of [C I] to ^{13}CO integrated line strengths

Figure 10 shows the observed correlation of the integrated intensities (in $[\text{K km s}^{-1}]$) of [C I] 1→0 (KOSMA data at 55''

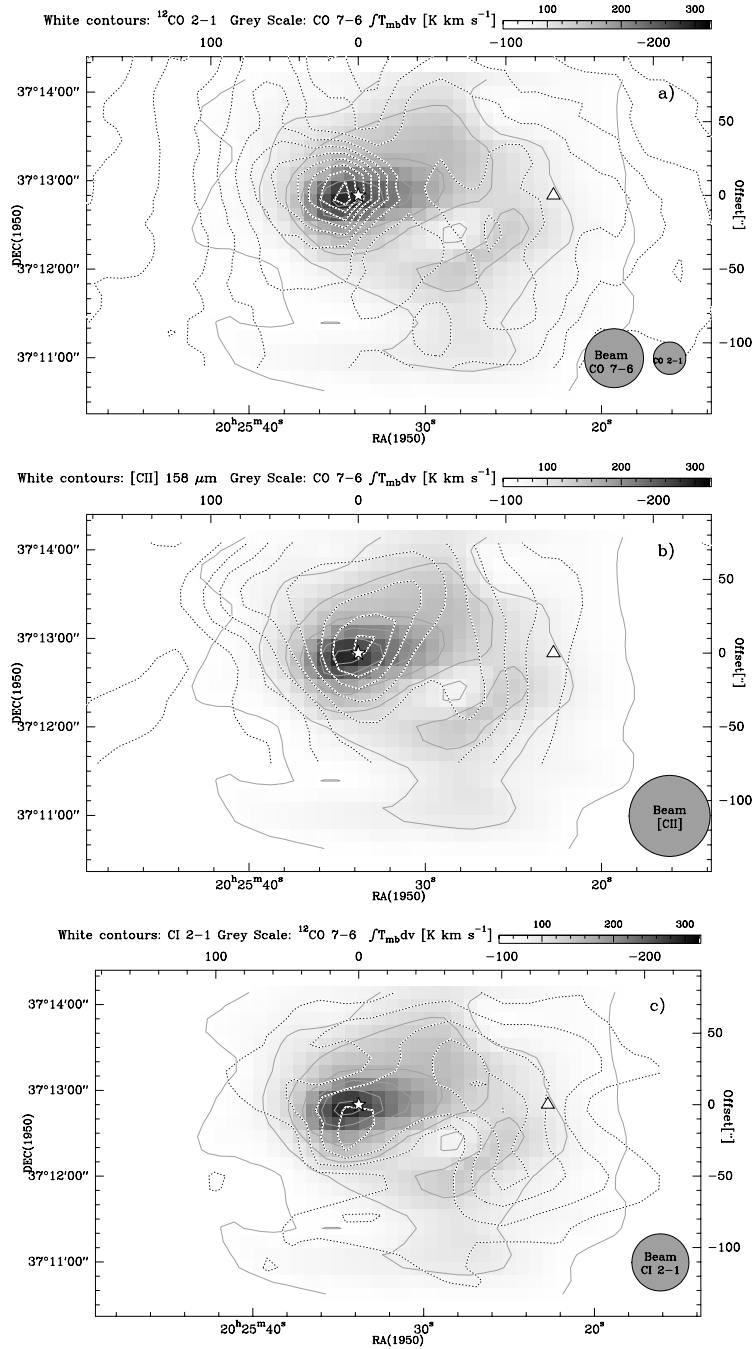


Fig. 9. Maps of the line integrated CO 7→6 emission (as a grey scale) overlaid with ^{12}CO 2→1 a), [CII] 158 μm b), [CI] 2→1 c) emission as white/dashed contours. The positions of S 106 IR is marked as a star and the ISO LWS position as a triangle. The contour ranges are (in the notation start/end/step): ^{12}CO 2→1 60/540/40 K km s^{-1} , [CII] 0.46/7.82/0.92 $\text{erg s}^{-1} \text{sr}^{-1} \text{cm}^{-2}$ ($2\sigma = 0.92 \text{ erg s}^{-1} \text{sr}^{-1} \text{cm}^{-2}$), [CI] 2→1 are 24/62/9.5 K km s^{-1} ($3\sigma = 12 \text{ K km s}^{-1}$), and CO 7→6 40/280/40 K km s^{-1} ($3\sigma = 13.5 \text{ K km s}^{-1}$).

resolution) and ^{13}CO 1→0 and 2→1 (IRAM data taken from Schneider et al. 2002, smoothed to 55'' angular resolution). The observed trends are described by a linear least-squares fit yielding a slope of 0.33 ± 0.05 for ^{13}CO 1→0 and 0.22 ± 0.03 for ^{13}CO 2→1. These slopes are shallower than those found by Ikeda et al. (1999) for ^{13}CO 2→1 in the Orion A cloud (~ 0.5) and by Plume et al. (1999) for an ensemble of clouds (W3, L1630, S140, and Cep A). A value of 0.8 was found by Tauber et al. (1994) for the Orion bar. For the relation to ^{13}CO 1→0, a slope of ~ 0.8 was given in Howe et al. (2000) for M 17.

4.4. A cut through the PDR of S 106

In this section, we discuss the excitation conditions derived from the observed molecular and atomic emission lines. We chose 7 positions along a cut at constant Declination with S 106 IR at 0,0 and give the line intensities and ratios in Table 3 and excitation temperatures and column densities in Table 4. Figure 11 illustrates the variation of the selected parameters along a slightly extended cut. The cut covers the two peak emission regions of the molecular cloud, east and

Table 3. Intensities and ratios (from the intensities in $\text{erg s}^{-1} \text{cm}^{-2} \text{sr}^{-1}$) of the observed atomic and molecular lines (ISO, KAO, KOSMA). All intensities are reported for $55''$ angular resolution, higher angular resolution data have been smoothed. Beam filling effects therefore to first order cancel out for the line ratios. *For these offsets, the [C I] 1 \rightarrow 0 line intensities and [C I] 1 \rightarrow 0/CO 4 \rightarrow 3 ratios are lower limits, and the [C I] 2 \rightarrow 1/1 \rightarrow 0 ratios upper limits due to possible self-chopping effects in the 1 \rightarrow 0 line.

Offset	120''	80''	40''	0	-40''	-80''	-120''
		*	East clump*	S 106 IR*			S 106 W
Intensities [$10^{-6} \text{ erg s}^{-1} \text{cm}^{-2} \text{sr}^{-1}$]							
[C II] 158 μm (KAO)	45	170	450	800	490	420	200
[O I] 63 μm (KAO)				7200			
[C I] 1 \rightarrow 0	1.10	1.78	2.21	2.17	2.25	2.56	2.79
[C I] 2 \rightarrow 1	6.8	12.0	16.1	26.4	25.0	26.6	29.0
CO 7 \rightarrow 6	15.6	37.5	56.9	121.4	83.7	72.0	58.0
CO 4 \rightarrow 3	2.4	4.85	10.3	14.4	12.6	9.7	9.5
Line ratios							
[O I] 63 μm /[C II] 158 μm KAO(ISO)				9(3.9)			-(0.4)
[O I] 145 μm /[C II] 158 μm (ISO)				0.67			0.074
[O I] 145 μm /[O I] 63 μm (ISO)				0.17			0.19
[C II] 158 μm (KAO)/CO 1 \rightarrow 0	237	607	1285	2424	1960	1555	740
[C I] 2 \rightarrow 1/[C I] 1 \rightarrow 0	6.2	6.75	7.3	12.2	11.1	10.4	10.4
[C I] 1 \rightarrow 0/CO 4 \rightarrow 3	0.47	0.37	0.22	0.15	0.18	0.26	0.29
CO 16 \rightarrow 15/CO 14 \rightarrow 13				0.44			
CO 7 \rightarrow 6/CO 4 \rightarrow 3	6.6	7.7	5.5	8.4	6.6	7.4	6.1
CO 2 \rightarrow 1/CO 1 \rightarrow 0	9.8	11.0	11.0	11.6	11.5	10.8	10.3

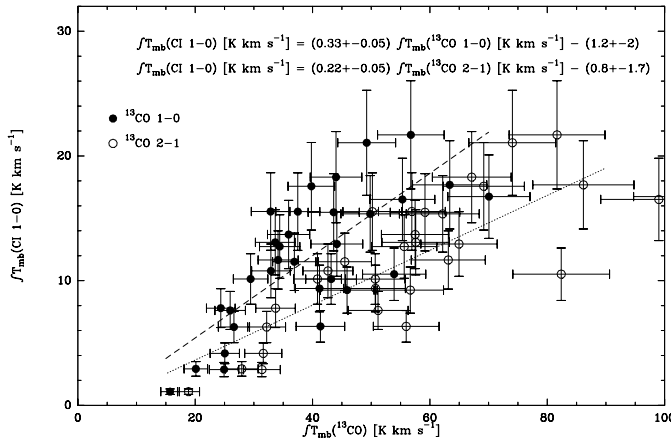


Fig. 10. Linear correlation of the integrated intensity of [C I] 1 \rightarrow 0 with ^{13}CO 1 \rightarrow 0 (filled circles) and ^{13}CO 2 \rightarrow 1 (open circles) at each position in S 106. The dashed lines show the least-squares fits to the data. The error bars indicate an assumed 20%(10%) uncertainty on the [C I] (^{13}CO) line integrated intensity.

west of S 106 IR, and the H II region/molecular cloud interface (refer to Fig. 2 or 6).

The calculation of these quantities is presented in the Appendix. For some line and column density ratios, we use isotomeric CO 2 \rightarrow 1 and 1 \rightarrow 0 data presented in Schneider et al. (2002). All observations were smoothed to $55''$ angular resolution and the CO column densities were recalculated

along the cut in this beam. In the following, we will discuss the values given in the tables together with Fig. 11.

Line intensities

From the distribution of the normalized intensities in Fig. 11a, we see that those lines requiring medium to high temperatures and/or densities (typically above 10^4 cm^{-3}) for excitation, i.e., [C II] and CO 7 \rightarrow 6, show a maximum at S 106 IR and fall off rapidly towards west and east. CO 4 \rightarrow 3 as an intermediate case shows also a peak at S 106 IR but the intensities decrease less rapidly away from the center. In contrast the ^{12}CO 2 \rightarrow 1 line, which is already excited in low density ($n < 10^4 \text{ cm}^{-3}$) and cool ($T < \text{a few ten K}$) gas, shows peak emission 20'' east of S 106 IR, falls off strongly towards the H II region (around offset $-40''$) and increases again to a flat maximum around $-120''$. Both [C I] lines do not peak at S 106 IR but at S 106 West (offset $-120''$) and show a rather flat emission distribution (the [C I] 1 \rightarrow 0 line more pronounced than [C I] 2 \rightarrow 1).

From the line strengths given in Tables 2 and 3 it is obvious that at the position of S 106 IR, the most important cooling line is [O I] 63 μm , followed by [O III] 52 μm (factor 2 weaker than [O I]) and [C II] 158 μm (1/3 of [O I] value). Other FIR atomic fine structure lines ([N III] 57 μm , [O I] 145 μm , [O III] 88 μm) follow before the high- J CO lines CO 15 \rightarrow 14, 14 \rightarrow 13, and 7 \rightarrow 6 (approx. 1/10 of the [O I] emission line

Table 4. Excitation conditions (excitation temperature, opacity, column density) derived from the observed FIR- and (sub)mm lines listed in Table 3 along a cut through S 106 IR. The last line gives the relative amount of material in each of the main carbon phases. *These values are lower limits since the beam filling is not known. †Upper limit for T_{ex} , adapted from high- J CO line ratio (Sect. 4.2).

Offset	120''	80''	40''	0	-40''	-80''	-120''
	East clump			S 106 IR	S 106 W		
Excitation temp. [K]							
$T_{\text{ex}}(\text{CO } 7 \rightarrow 6)^*$	20	23	35	50	41	40	38
$T_{\text{ex}}([\text{C I}] 2 \rightarrow 1 / [\text{C I}] 1 \rightarrow 0)$	60	70	80	500 [†]	410	320	150
Opacity							
$\tau([\text{C I}] 1 \rightarrow 0)$	0.1	0.1	0.1	0.01	0.01	0.02	0.04
$\tau([\text{C I}] 2 \rightarrow 1)$	0.1	0.1	0.1	0.02	0.02	0.03	0.1
Column densities [10^{17} cm^{-2}]							
$N([\text{C I}])$	1.27	2.10	2.67	3.05	3.09	3.53	3.63
$N([\text{C II}])$	0.28	1.07	2.83	5.04	3.09	2.65	1.26
$N(^{13}\text{CO})$	0.71	1.42	1.57	1.10	0.75	0.95	1.10
$\text{C}^+:\text{C}^0:\text{CO}$	1:3:96	1:3:96	3:3:94	8:5:87	7:7:86	5:7:88	2:8:90

strength). The $[\text{C I}] 2 \rightarrow 1$ and $\text{CO } 16 \rightarrow 15$ lines have the same intensity and are still important coolants. At the other positions along the cut (however, with less tracers to compare), the most important cooling line is always $[\text{C II}]$, followed by $\text{CO } 7 \rightarrow 6$ and $[\text{C I}] 2 \rightarrow 1$ (approximately a factor 2–3 weaker than CO). Since the optical depth of $[\text{C I}] 2 \rightarrow 1$ is small (≤ 0.1), as is presumably that of the $[\text{C II}]$ line (see Appendix), but the lines are quite bright, the emission from these lines arises probably from several compact/condensed slabs along the line of sight.

Excitation temperatures

The variation of the excitation temperature, derived from the two CO lines, and the $[\text{C I}] 2 \rightarrow 1 / 1 \rightarrow 0$ line ratio is shown in Fig. 11b. Values for T_{ex} derived from the $[\text{C I}]$ line ratio are not affected by beam filling but have a large error ($\sim 30\text{--}40\%$) due to possible errorbeam pickup and self-chopping. To partly account for the errorbeam pickup in the $[\text{C I}] 2 \rightarrow 1$ line, we reduced its intensity by 15%. In addition, we adapted $T_{\text{ex}} = 500 \text{ K}$ (derived from the ISO high- J CO line ratio and from the literature, see Sect. 4.2) as a maximum value towards S 106 IR. The $[\text{C I}]$ line ratio $2 \rightarrow 1 / 1 \rightarrow 0$ gave an excitation temperature of around 650 K. The excitation temperatures derived from the $\text{CO } 7 \rightarrow 6$ and $4 \rightarrow 3$ lines are lower limits since the beam filling is assumed to be unity. Accordingly, the absolute values are lower than the ones obtained by the $[\text{C I}]$ line ratio. In any case, the maximum of T_{ex} is found towards S 106 IR with a sharp decrease in excitation temperature towards the east and a much smoother decline towards the western part of the cloud.

Line ratios

Selected integrated line intensity ratios (from the intensities in $[\text{K km s}^{-1}]$) are displayed in Fig. 11c. The most prominent feature is the strong enhancement of the $[\text{C I}] 2 \rightarrow 1 / 1 \rightarrow 0$

ratio at the position of S 106 IR which stays at a high level between S 106 IR and the NH_3 peak. Generally, the line integrated ratio $[\text{C I}] 2 \rightarrow 1 / 1 \rightarrow 0$ varies between 1 and 1.8 along the cut. However, this is an *upper* limit due to the errorbeam pickup of the $[\text{C I}] 2 \rightarrow 1$ line and possible self-chopping in the $[\text{C I}] 1 \rightarrow 0$ line. This high ratio is accompanied by a decrease of the $[\text{C I}] 1 \rightarrow 0 / \text{CO } 7 \rightarrow 6$, $[\text{C I}] 1 \rightarrow 0 / \text{CO } 4 \rightarrow 3$, and $[\text{C I}] 1 \rightarrow 0 / \text{CO } 3 \rightarrow 2$ ratio. The apparent depopulation of the $[\text{C I}] 3\text{P}_1$ level is thus due to high temperatures, favouring the population of the medium to high- J CO levels and the higher lying $[\text{C I}] 3\text{P}_2$ state. Hence, there must be a dense and hot gas component towards S 106 IR, a conclusion readily supported by the mere detection of the $\text{CO } 16 \rightarrow 15$, $15 \rightarrow 14$, and $14 \rightarrow 13$ lines (see Sect. 4.2.).

The line ratio for $[\text{C I}] 1 \rightarrow 0 / \text{CO } 3 \rightarrow 2$ varies between 0.09 and 0.17 and for $[\text{C I}] 1 \rightarrow 0 / \text{CO } 4 \rightarrow 3$ between 0.12 and 0.38, which shows that generally the CO lines are more efficient coolants for the gas than the $[\text{C I}] 1 \rightarrow 0$ line. Typical values for other PDRs of $[\text{C I}] 1 \rightarrow 0 / \text{CO } 3 \rightarrow 2$ are 0.3–0.4 for W51 A/B (Arikawa et al. 1999), 0.15–0.80 in Orion A (Tatematsu et al. 1999), and 0.2–0.8 for M 17 (Sekimoto et al. 1999), where a similar gradient varying with excitation temperature was found. The average Galactic value is 0.57, determined from *COBE* FIRAS data (Fixsen et al. 1999), so that in comparison with other bright and more massive Galactic PDRs, S 106 contributes less to the overall Galactic $[\text{C I}]$ emission. The $[\text{C I}] 1 \rightarrow 0 / ^{13}\text{CO } 1 \rightarrow 0$ line ratio varies only little between 0.23 and 0.48 along the cut and is also almost independent of the UV field. This ratio hence traces a cooler gas component in which the $[\text{C I}] 1 \rightarrow 0$ and the low to medium- J CO lines are sufficiently excited. Typical values for other externally illuminated PDRs are slightly higher (0.6–0.8 for Orion, Ikeda et al. 1999). PDRs in external galaxies have values of typically 0.16–0.47 (e.g. M 83, Petitpas & Wilson 2001). The $[\text{C I}] 1 \rightarrow 0 / \text{CO } 2 \rightarrow 1$ ($\text{CO } 1 \rightarrow 0$) ratio in galaxies is on average 0.2 with a spread of 0.1–1.0 (nucleus of NGC 6946 and M 83,

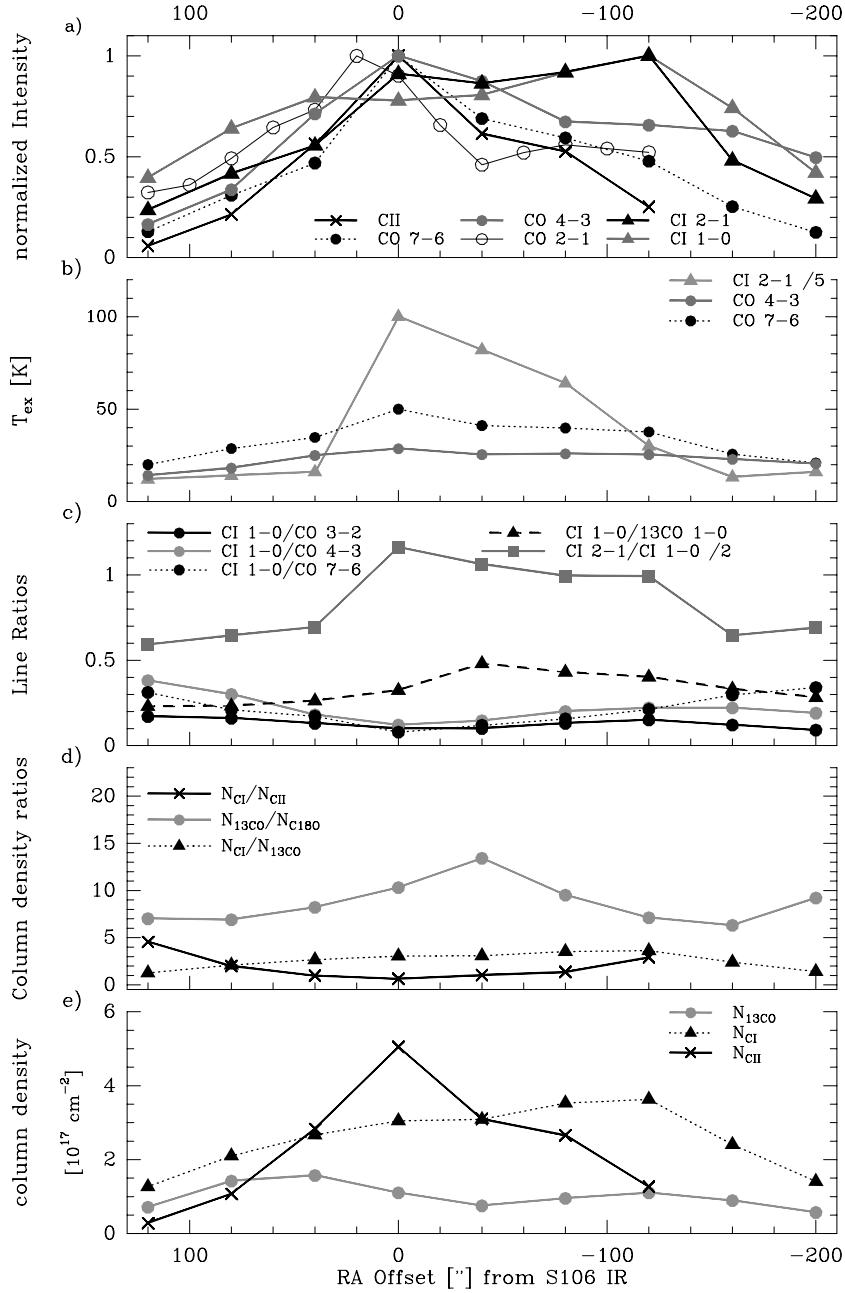


Fig. 11. The top panel **a)** shows the normalized line integrated intensities (in [$\text{erg s}^{-1} \text{sr}^{-2} \text{cm}^{-2}$]) of [C II] 158 μm , [C I] 2 \rightarrow 1 and 1 \rightarrow 0, and ^{12}CO 7 \rightarrow 6, 4 \rightarrow 3, and CO 2 \rightarrow 1 (all at 55'' resolution) along an east-west cut at the Declination of the star S 106 IR. The typical errors of the intensities are around 5% for the [C II] and low- J CO lines, and around 15%–20% for the [C I] and medium- J CO lines. The following panels display excitation temperatures **b)**, integrated line intensity ratios with the intensities in K kms^{-1} **c)**, column density ratios **d)**, and column densities **e)**. The line ratio [C I] 2 \rightarrow 1/1 \rightarrow 0 is displayed a factor of 2 weaker and T_{ex} derived from this ratio a factor of 5 weaker than the actual values.

Israel & Baas 2001 and Gerin & Phillips 2000 for a selection of galaxies of different type).

Column densities and ratios

The column density ratios $N([\text{C I}])/N([\text{C II}])$, $N(^{13}\text{CO})/N(\text{C}^{18}\text{O})$, $N([\text{C I}])/N(^{13}\text{CO})$ and the absolute values of the ^{13}CO , [C I], and [C II] column densities (in [cm^{-2}]) are shown in Figs. 11d and 11e.

From the variation of the column densities and ratios we see that:

(i) The $N([\text{C I}])/N([\text{C II}])$ ratio has a flat minimum at the position of S 106 IR. The [C II] column density peaks at S 106 IR, indicating that it is the position with the largest amounts of hot PDR gas. In contrast to that, the [C I] column density peaks at S 106 W and has only a secondary peak at S 106 IR. The absolute values of the [C I] column density are 4 times larger than the ^{13}CO column density at S 106 W and

only 2 times larger at offset 40'' (“east clump”). The largest amount of molecular gas is therefore found in the east, whereas the western region is dominated by PDR gas.

(ii) The $N([\text{C I}])/N(^{13}\text{CO})$ ratio varies between 1–4 along the cut. This translates into a $N([\text{C I}])/N(^{12}\text{CO})$ ratio of 0.04–0.1 if we assume a $[^{12}\text{CO}/^{13}\text{CO}]$ abundance of 50 (Howe et al. 2000). This is close to the value of 0.1 found by Plume et al. (2000) for Orion A but lower than the average value of 0.37 derived by Howe et al. (2000) for M 17. The absolute values of the [C I] column densities show little variation ($2.7\text{--}3.6 \times 10^{17} \text{ cm}^{-2}$ if we exclude the two easternmost positions likely affected by self-chopping) and therefore are mainly independent of the UV field and the density. The [C I] column density is only weakly dependent on the excitation temperature. For example, a change of T_{ex} from 80 to 30 K at the position of the East clump decreases the column density by only 20%. A constant [C I] column density at a value of $\sim 2 \times 10^{17} \text{ cm}^{-2}$ is predicted by single-sided, plane-parallel PDR models (Tielens & Hollenbach 1985; Hollenbach et al. 1991). Our column densities are slightly higher, indicating that the [C I] emission arises probably from several PDR surfaces along the line of sight. Chemical models (Pineau de Forêts et al. 1992) predict also a constant [C I] column density and a [C I]/CO column density ratio of 0.1–0.2 for low densities ($< 5.5 \times 10^3 \text{ cm}^{-3}$) and ≤ 0.01 for higher densities in the cloud cores.

(iii) The $N(^{13}\text{CO})/N(\text{C}^{18}\text{O})$ ratio is equal to or larger than 7 along the whole cut with a maximum at $-40''$ west of S 106 IR. A ratio > 7 (the natural isotopic abundance, Langer & Penzias 1990) indicates a strong UV field since the more abundant ^{13}CO is effectively self-shielding. This effect is enhanced if the medium is clumpy on small scales ($< 0.2 \text{ pc}$), because small clumps provide even less column density for the C^{18}O molecule to be protected against dissociation.

4.4.1. The amount of carbon in the main phases C^+ , C^0 , CO

From the [C II], [C I] and ^{13}CO column densities given in Table 4, and assuming a $[^{12}\text{CO}/^{13}\text{CO}]$ ratio of 50, we can determine the number of atoms/molecules along the cut in a $55''$ beam and finally the fractional abundance of carbon in each of the three main carbon phases ($\text{C}^+:\text{C}^0:\text{CO}$). The CO region is dominating the whole cut with more than 86% of the total gas-phase carbon towards all positions. Even at the location of S 106 IR – the position with the highest column density of [C II] – the $\text{C}^+:\text{C}^0:\text{CO}$ ratio remains 8:5:87. Typical values for other PDR regions are 40:10:50 (NGC 2024, Jaffe & Plume 1995) and 37:7:56 (IC 63, Jansen et al. 1996), indicating a larger amount of ionized and atomic carbon in the PDR region. It should be noted that the CO column density is an upper limit (Schneider et al. 2002) and might be a factor 2–5 smaller than the value given here.

An upper limit for the total carbon abundance can be derived using the visual extinction and assuming that the

CO emitting region is located in the foreground. An extinction $A_v = 14^m$ (van den Ancker et al. 2000) corresponds to a total hydrogen column density of $N(\text{H}+\text{H}_2) = 14/3.1 \times 5.8 \times 10^{21} \text{ cm}^{-2} = 2.6 \times 10^{22} \text{ cm}^{-2}$. The total carbon column density is $N(\text{C}) = 6.3 \times 10^{18} \text{ cm}^{-2}$ so that the carbon abundance is $\text{C}/\text{H} = 2.4 \times 10^{-4}$. This value compares reasonably well with the fractional abundance of 3.6×10^{-4} in the solar neighborhood (Anders & Grevesse 1989) and the value 3×10^{-4} used in PDR models (Tielens & Hollenbach 1985; Hollenbach et al. 1991; Sternberg & Dalgarno 1989), based upon observations in Orion and ρ Oph (see references in Tielens & Hollenbach 1985). Values for the C/H_2 ratio in cold dark clouds are smaller (typically around $1\text{--}2 \times 10^{-5}$, Frerking et al. 1989; Keene 1997).

Summarizing the analysis so far, it is evident that the emission properties and the distribution of the [C II], and high- J ($J_{\text{up}} > 6$) CO lines differ significantly from the [C I] $2 \rightarrow 1$ and $1 \rightarrow 0$, and low to medium- J ($J_{\text{up}} \leq 6$) CO lines. This reflects either a density and temperature gradient within more or less homogeneous clouds around S 106 IR and S 106 NH₃, or supports a two-phase gas model in which high density clumps with a high surface temperature (generated by the strong UV field of S 106 IR) are embedded in lower density interclump gas.

5. Comparison with a PDR model

In order to constrain the densities and the UV field along the cut, we applied some of the observed intensities and line ratios to the PDR model of Kaufman et al. (1999). Those lines and ratios were selected for which we obtained model output data via the internet (see Fig. 12). The model uses an escape probability formalism for a one-dimensional semi-infinite slab with constant density. Figure 12 shows the results for the positions of S 106 IR and S 106 W. All data are smoothed to the same angular resolution of $55''$ before being applied to the model, except the [O I] 145/[C II] 158, ratio, which was observed with the $80''$ ISO beam. All line intensities are given in $[\text{erg s}^{-1} \text{ sr}^{-1} \text{ cm}^{-2}]$, line ratios are derived from these.

Various line ratios are shown in the plot, we also calculated a reduced χ^2 which was determined from the line ratios and weighted with the individual uncertainties.

5.1. The position of S 106 IR

For S 106 IR, the observed line ratios do not yield a common, well constrained density and temperature range ($\chi^2 \gg 1$). In order to restrict at least the UV field, we determined G_0 in other ways:

van den Ancker et al. (2000) used two independent approaches to estimate the FUV field: first, they derived $G_0 \geq 10^5$ from their ISO observations of FIR [Si II] and [Fe II] lines using a plane-parallel, homogeneous PDR model (Tielens & Hollenbach 1985). Second, they determined a spectral type O8 for S 106 IR from a photo-ionization code (Ferland 1996) with models for a stellar atmosphere (Kurucz 1991) and using atomic fine structure line ratios. Such a star emits typically $3.6 \times 10^{36} \text{ erg s}^{-1} \text{ sr}^{-1}$ which is diluted to $10^5\text{--}10^6 G_0$ at

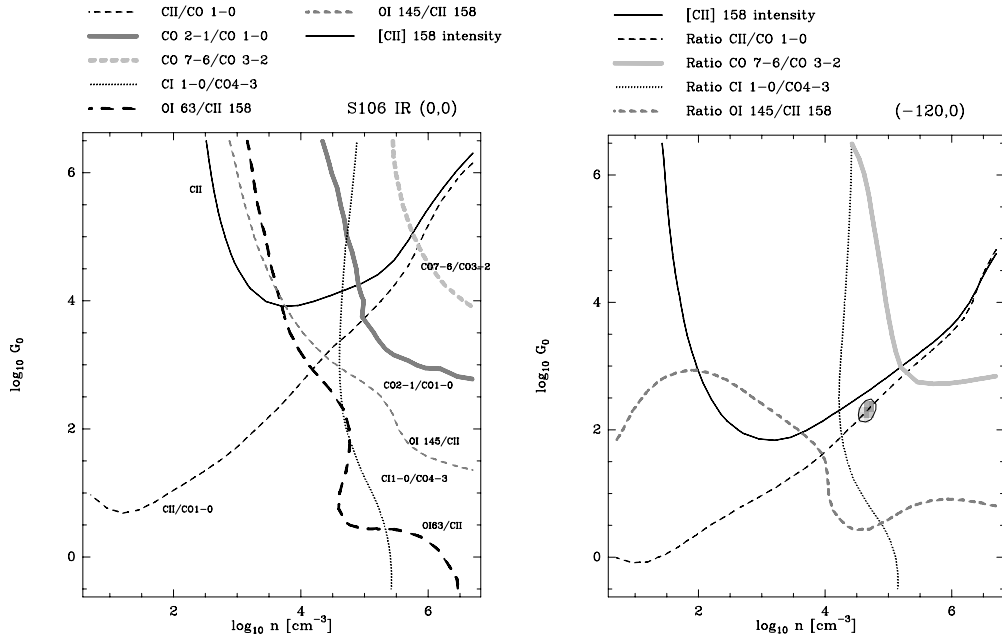


Fig. 12. Various FIR- and Submm molecular and atomic line ratios observed at S 106 IR (*left*) and S 106 W ($-120'', 0$) (*right*) are displayed within a parameter space for density and UV flux based upon a PDR-model from Kaufman et al. (1999). The plot for S 106 W shows as a grey scale the distribution of the reduced χ^2 . The contour level indicates the 1σ standard deviation of the minimum χ^2 .

a (projected) geometrical distance of 0.015 to 0.05 pc (angular distance 5–17'').

We used a third approach by determining the color temperature T_0 derived from the $50\ \mu\text{m}$ to $100\ \mu\text{m}$ intensity ratio $I(50\ \mu\text{m})/I(100\ \mu\text{m})$ (Sect. 4.1) and applied it to the model of Hollenbach et al. (1991) in which T_0 becomes a function of G_0 . The ratio within an area of $3/5$ diameter centered on S 106 IR is 1.2. This implies a dust color temperature of 56 K for an assumed dust emissivity law of λ^{-1} . By using Fig. 19 of Hollenbach et al. (1991) in which the slightly different ratio $I(60\ \mu\text{m})/I(100\ \mu\text{m})$ is given as a function of G_0 , we obtain an UV flux of $(1-2) \times 10^5 G_0$.

A resulting UV field of a few $10^5 G_0$ indicates two density regimes in Fig. 12. One is found around $10^3\ \text{cm}^{-3}$, marked by the $[\text{O I}] 63/[\text{C II}]$ and $[\text{O I}] 145/[\text{C II}]$ line ratio. Since the critical density of the $[\text{C II}]$ line is only a few $10^3\ \text{cm}^{-3}$, there might be a PDR layer at that density. However, this layer can not be the origin of the high- J CO lines since they have much higher critical densities. Therefore, the density regime (a few times $10^5\ \text{cm}^{-3}$) which is defined by the $\text{CO } 7\rightarrow 6/\text{CO } 3\rightarrow 2$ and $[\text{C II}]/\text{CO } 1\rightarrow 0$ line ratio and $[\text{C II}]$ intensity is more realistic for the high- J CO lines. (We do not consider the $\text{CO } 2\rightarrow 1/\text{CO } 1\rightarrow 0$ ratio because the lines do not originate in the hot PDR gas characterized by the strong UV field.) Since the beam filling factor for the $[\text{C II}]$ line emission is not known, the $[\text{C II}]$ intensity is not well suited to constrain the physical parameters of the PDR gas.

The observed high $[\text{C I}] 2\rightarrow 1/1\rightarrow 0$ line ratio (not appearing in the plot because the contour lies out of the defined range) points to even higher densities and UV field. Due to possible self-chopping effects in the $[\text{C I}] 1\rightarrow 0$ line, however, a reduced (typically by 20%) ratio is likely to be more appropriate and is in accord with those line ratios indicating high densities and

UV field. The same argument holds for the $[\text{C I}] 1\rightarrow 0/\text{CO } 4\rightarrow 3$ ratio which is also shifted towards higher densities in case of a stronger $[\text{C I}]$ line. The density values obtained with the PDR model are in good accordance with what we obtained from the escape probability model (Sect. 4.2) where we derive plausible densities between $3 \times 10^5\ \text{cm}^{-3}$ (at 500 K) and $5 \times 10^6\ \text{cm}^{-3}$ (at 200 K). Graf et al. (1993) obtained a density of $3 \times 10^5\ \text{cm}^{-3}$ from $\text{CO } 14\rightarrow 13$ observations with the KAO. The remaining line ratios define a regime of lower density ($\sim 3 \times 10^4\ \text{cm}^{-3}$) and UV field ($> 10^3 G_0$) which probably traces another excitation phase of the gas (see above).

Putting these findings together, we conclude that the plane-parallel, homogeneous PDR model alone is not suitable to explain all observed lines and line ratios at the location of S 106 IR. This is not surprising because a single density/temperature gas phase close to S 106 IR would be physically implausible. In the immediate environment of the star, we find evidence for the existence of hot, UV bathed PDRs on the surfaces of cold, dense clumps so that a whole range of densities and temperatures is to be expected. In addition, the gas is highly dynamic due to the stellar wind and probably more clumpy (see below) than in the remote part of the cloud.

5.2. S 106 west and other positions along the cut

In contrast to S 106 IR, we find for S 106 W (Fig. 12) fairly well constrained values for the density and UV field ($\chi^2 \sim 1.75$). For the remaining positions, we can only use the available line ratios $[\text{C II}]/\text{CO } 1\rightarrow 0$, $\text{CO } 7\rightarrow 6/3\rightarrow 2$, $[\text{C I}] 2\rightarrow 1/1\rightarrow 0$, and $[\text{C I}] 1\rightarrow 0/\text{CO } 4\rightarrow 3$ and the $[\text{C II}]$ line intensity. The χ^2 for the remaining positions has values of 2.7 (120''), 3.4 (offset 80''), 3.5 (40''), 2.6 (−40''), and 3.4 (−80'') which implies (similar to S 106 IR) not well constrained values for density

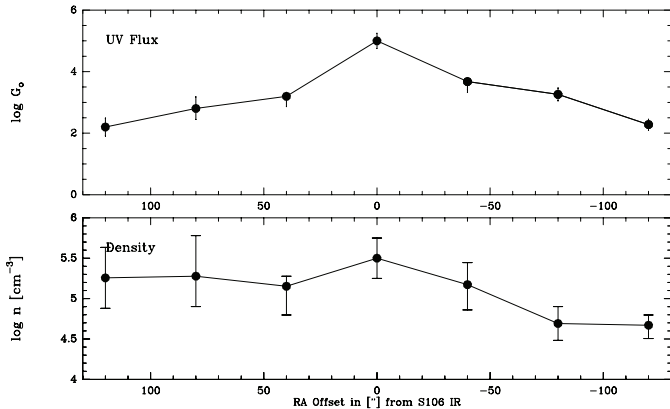


Fig. 13. The UV flux (*top*) and particle density (*bottom*) along the cut obtained by comparing the observed data with the PDR model of Kaufman et al. (1999).

and UV field. However, it should be noted that in particular the [C I] 2→1/1→0, CO 7→6/3→2 and [C I] 1→0/CO 4→3 line ratios are not well determined (due to error-beam pickup and/or self-chopping). A larger error ($\geq 30\%$) for these quantities reduces the χ^2 to values between 1 and 2. In the following, we use the results from the PDR models to obtain at least an estimate for densities and UV field along the cut.

5.3. Density and UV flux from the model

The variations of UV flux and density, derived from the PDR model, are shown in Fig. 13. The error bars are calculated from the 1σ standard deviation of the reduced χ^2 value (see Fig. 12). Considering the error bars, it is evident that the density is roughly constant with a value around 10^5 cm^{-3} in the east and $10^{4.5} \text{ cm}^{-3}$ in the west. This finding is fully consistent with the results of Schneider et al. (2002), where the observed low- J CO emission was found as arising from rather homogeneous, low-density, and spatially extended clumps. The typical clump size was determined to be $1/2$ and the local density within the clumps $9 \times 10^4 \text{ cm}^{-3}$. In particular the region *east* of S 106 IR is dominated by emission from rather homogeneous molecular gas, i.e., large clumps (0.2–0.3 pc) like the “East clump”, traced by low- J CO lines and [C I] 1→0, significantly attenuating the UV radiation from S 106 IR. The spatial extent of the [C II], [C I] 2→1, and medium- J CO lines, however, indicates that the molecular cloud structure must be clumpy to a certain degree in order to enable the penetration of UV radiation. The UV field shows a stronger variation, gradually increasing from $\approx 100 G_0$ at the eastern and western border to a maximum of a few $10^5 G_0$ at the position of S 106 IR. Generally, the UV field decreases faster than the pure geometrical $1/r^2$ dilution away from S 106 IR, especially on the East side. This indicates that the illuminated clouds are located at a distance larger than the projected one.

We therefore arrive at the same conclusion as in the preceding S 106 paper (Schneider et al. 2002), namely that high density clumps are embedded in a low to medium dense phase and that close to S 106 IR, the gas is probably more clumpy than in the more remote parts of the cloud. In addition, we

see a difference between the region west and east of S 106 IR: the correlation of the emission distributions of the ^{13}CO 2→1 and [C I] 1→0 lines (^{13}CO 2→1 looks less structured west of S 106 IR where [C I] 1→0 emits stronger) and the increasing $N(^{13}\text{CO})/N(\text{C}^{18}\text{O})$ ratio in the west both indicate a higher degree of clumpiness compared to the east. This scenario is also supported by the CN and CS observations on smaller scales discussed in Sect. 3.3.2.

6. Summary

We have presented a spectroscopic study of the molecular cloud associated with S 106 in submm rotational transitions of ^{12}CO 7→6 and ^{12}CO 4→3, obtained with the KOSMA 3m, and CN $N = 3 \rightarrow 2$ and CS 7→6, observed with the JCMT 15-m radio telescopes.

For the investigation of the associated photon dominated region, which is created by the exciting star S 106 IR, we observed the [C II] 158 μm and [O I] 63 μm fine structure lines with the KAO and the [C I] 2→1 and 1→0 lines with KOSMA. ISO LWS grating scans were taken at two positions (S 106 IR and 120'' west) and are discussed and compared to the KAO observations. The results of this study are summarized as follows:

1. The large scale extent of the PDR ($10' \times 3'$) was determined from $\sim 50''$ angular resolution [C II] 158 μm , [C I] 1→0 and 2→1, and CO 7→6 and 4→3 mapping. [C II], CO 7→6 and 4→3 show an unresolved peak at the location of S 106 IR, whereas the [C I] maps show an additional maximum around 120'' west of S 106 IR (named S 106 W), close to an NH_3 peak.

A smaller 22'' resolution [O I] 63 μm map around S 106 IR shows peak emission associated with a prominent feature of the molecular cloud, the “East Clump”. The peak intensity of the [O I] line of $2.1 \times 10^{-2} \text{ erg s}^{-1} \text{ cm}^{-2} \text{ sr}^{-1}$ at the position of S 106 IR is much higher than the [C II] peak intensity of $8 \times 10^{-4} \text{ erg s}^{-1} \text{ cm}^{-2} \text{ sr}^{-1}$.

2. The ISO LWS grating scans taken at S 106 IR and S 106 W show (i) a significant variation in intensities for the [C II] and [O I] lines and (ii) that the high- J CO lines ($14 \leq J_{\text{up}} \leq 16$) are only excited at S 106 IR. This implies higher densities and a stronger UV field at S 106 IR. From the line strengths, we obtain that the [O I] 63 μm line is the most important cooling line at S 106 IR, followed by other atomic FIR lines ([O III] 52 μm , [C II] 158 μm) and high- J CO lines.

3. An intercomparison between the observed maps reveals a good morphological correlation between CO 7→6, [C I] 2→1, and [C II], marking the hottest part of the PDR at S 106 IR, and [C I] 1→0 and ^{13}CO 2→1, showing the typical double peak emission distribution of the molecular cloud with a tendency to avoid regions of high density and temperature close to the exciting star. A linear least-squares fit to the observed correlation of the integrated intensities between [C I] 1→0 and ^{13}CO 1→0 (2→1) yields a slope of 0.33 ± 0.05 (0.22 ± 0.03). These values are lower than those observed in other star forming regions.

4. The molecular cloud structure in the PDR/molecular cloud transition zone immediately around S 106 IR ($1' \times 1'$)

is revealed in 14'' resolution JCMT CN $N = 3 \rightarrow 2$ and CS $J = 7 \rightarrow 6$ maps: the CN emission has two peaks on small scales, the East clump and S 106 FIR, but also outlines features in the more quiescent eastern part of the cloud seen in $^{13}\text{CO } 2 \rightarrow 1$ line (e.g., associated with the dark dust lane). CS emission is more confined to and peaks closer to the side of the east clump facing S 106 IR.

5. We obtain an upper limit to the flux ratio $F_{\text{CII}}/F_{\text{FIR}}$ of 6.75×10^{-3} or 0.7%, which is slightly higher than typical values ($1-3 \times 10^{-3}$) for Galactic star forming regions.

6. From the CO $16 \rightarrow 15/\text{CO } 14 \rightarrow 13$ line ratio and the CO $7 \rightarrow 6$ intensity at the position of S 106 IR, we determine a range of possible temperatures between 200 and 500 K and densities between $5 \times 10^6 \text{ cm}^{-3}$ and $3 \times 10^5 \text{ cm}^{-3}$. The CO column density divided by the line width ($N_{\text{CO}}/\Delta\nu$) stays constant around $6 \times 10^{17} \text{ cm}^{-2}/(\text{km s}^{-1})$. These values are consistent with estimates from the literature (Harris et al. 1987; Richer et al. 1993; Graf et al. 1993; van den Ancker et al. 2000).

7. We discuss line intensities and ratios and the variation of the excitation temperature T_{ex} , opacities, column densities, and column density ratios along a cut at constant Declination with S 106 IR at the center. We find that the $[\text{C I}] \ ^3\text{P}_1$ level is depleted due to high temperatures, favouring the population of the higher lying $[\text{C I}] \ ^3\text{P}_2$ state and the medium to high- J CO levels. The ratios for $[\text{C I}] \ 1 \rightarrow 0/\text{CO } 3 \rightarrow 2$, $[\text{C I}] \ 1 \rightarrow 0/\text{CO } 4 \rightarrow 3$, and $[\text{C I}] \ 1 \rightarrow 0/^{13}\text{CO } 1 \rightarrow 0$ vary between 0.1 and 0.2, 0.1 and 0.4, and 0.2 and 0.5, respectively. This indicates that the CO lines are more efficient coolants for the gas than the $[\text{C I}] \ 1 \rightarrow 0$ line. Since the average Galactic value of $[\text{C I}] \ 1 \rightarrow 0/\text{CO } 3 \rightarrow 2$ is 0.57 (COBE FIRAS), the S 106 region contributes less to the overall Galactic $[\text{C I}]$ emission compared to other bright and more massive Galactic PDRs. From the absolute values and the variation of the column densities $N([\text{C I}])$, $N([\text{C II}])$, $N(^{13}\text{CO})$, and $N(\text{C}^{18}\text{O})$, we conclude the following: At S 106 IR, we find the largest amounts of hot gas; the $N([\text{C I}])/N(^{13}\text{CO})$ ratio varies between 1 and 4 whereas the $[\text{C I}]$ column density is rather constant (around $3 \times 10^{17} \text{ cm}^{-2}$ along the cut and therefore independent of density and UV field. The $N(^{13}\text{CO})/N(\text{C}^{18}\text{O})$ ratio is larger than the natural isotopic abundance (~ 7) which indicates a strong UV field (self-shielding of ^{13}CO).

9. We applied the observed FIR and CO line intensities and ratios to a plane-parallel PDR model along a cut at constant Declination through S 106 IR. We obtain that the PDR model is not well suited to explain the observed intensities since we probably observe several PDRs along the line of sight. In a first order estimate, however, we find that the UV field gradually decreases from a few $10^5 G_0$ at S 106 IR to approximately $10^2 G_0$ at 120'' (0.35 pc) distance. The density distribution is flatter with values around 10^5 cm^{-3} at all positions along the cut except for S 106 IR ($n > 3 \times 10^5 \text{ cm}^{-3}$).

10. The emission properties and the distribution of the $[\text{C II}]$, $[\text{C I}] \ 2 \rightarrow 1$, and high- J ($J_{\text{up}} \geq 7$) CO lines differ significantly from the $[\text{C I}] \ 1 \rightarrow 0$, and low to medium- J ($J < 5$) CO lines. This leads us to the conclusion that the gas in the S 106 region consists of two phases: small ($\ll 0.2$ pc), high density clumps close to S 106 IR with a high surface temperature (due to the strong UV field of the star), embedded in low-

medium density gas, which is spatially more extended, dynamically less active, and probably less clumpy than in the remote part of the cloud.

Acknowledgements. We thank the FIFI team, A. Poglitsch, Norbert Geis, Thomas Nicola, and Ralf Timmermann, and the KAO crew for the competent support. A part of the $[\text{C I}]$ observations was performed by S. Heyminck.

We would like to thank the referee M. Gerin for useful comments which improved the paper.

This work was supported by the Deutsche Forschungsgemeinschaft (DFG) through grant SFB-494.

The KOSMA 3m submillimeter telescope at the Gornegrat-Süd is operated by the University of Cologne in collaboration with Bonn University, and supported by special funding from the Land NRW. The observatory is administered by the International Foundation Gornegrat and Jungfrauoch.

Based on observations with ISO, an ESA project with instruments funded by ESA Member States (especially the PI countries: France, Germany, the Netherlands and the United Kingdom) and with the participation of ISAS and NASA. The ISO Spectral Analysis Package (ISAP) is a joint development by the LWS and SWS Instrument Teams and Data Centers. Contributing institutes are CESR, IAS, IPAC, MPE, RAL and SRON.

References

- Anders, E., & Grevesse, N. 1989, *Geochim. Cosmochim. Acta* (ISSN 0016-7037), 53, 197
- Arikawa, Y., Tatematsu, K., & Sekimoto, Y. 1999, *Proceedings of Star Formation 1999*, Japan, June 21–25, 1999, ed. T. Nakamoto (Nobeyama Radio Observatory), 88
- Bally, J., & Scoville, N. Z. 1982, *ApJ*, 255, 497
- Clegg, P., Ade, P. A. R., Armand, C., et al. 1996, *A&A*, 315, L38
- Cole, D. M. 1997, *A&AS*, 191, 12906
- Eiroa, C., Elsässer, H., & Lahulla, J. F. 1979, *A&A*, 74, 89
- Fixsen, D. J., Bennett, C. L., & Mather, J. C. 1999, *ApJ*, 526, 207
- Ferland, G. J. 1996, *Univ. of Kentucky Physics Department Internal Report*
- Frerking, M., Keene, J., Blake, G., & Philipps, T. 1989, *ApJ*, 344, 311
- Furuya, A. R., Kitamura, Y., Claussen, M., et al. 1999, *A&AS*, 194, 5013
- Gehrz, R., Grasdalen, G., Castelaz, M., et al. 1982, *ApJ*, 254, 550
- Genzel, R., Harris A., & Stutzki, J. 1989, *ESA, IR Spectroscopy in Astronomy*, 115
- Gerin, M., & Phillips, T. G. 2000, *ApJ*, 537, 644
- Graf, U., Eckart, A., Genzel, R., et al. 1993, *ApJ*, 405, 249
- Graf, U., Heyminck, S., Michael, E. A., et al. 2002, *Proc. of the 13th Intern. Symp. on Space THz Technology*
- Griffin, M. J., Ade, P. A. R., & Orton, G. S. 1986, *Icarus*, 65, 244
- Harris, A. I., Stutzki, J., Genzel, R., et al. 1987, *ApJ*, 322, L49
- Harvey, P. M., Gatley, I., Thronson, H. A., et al. 1982, *ApJ*, 258, 568
- Hodapp, K., & Rayner, J. 1991, *AJ*, 102, 1108
- Hogerheijde, M. R., Jansen, D. J., & vanDishoeck, E. F. 1995, *A&A*, 294, 792
- Hollenbach, D., Takahashi, T., & Tielens, A. 1991, *ApJ*, 377, 192
- Howe, J. E., Jaffe, D., Genzel, R., & Stacey, G. 1991, *ApJ*, 373, 158
- Howe, J. E., Ashby, M. L. N., Bergin, E. A., et al. 2000, *ApJ*, 539, L137
- Israel, F. P., & Baas, F. 2001, *A&A*, 371, 433
- Ikeda, M., Maezawa, H., Ito, T., et al. 1999, *ApJ*, 527, L59
- Jaffe, D. T., Harris, A. I., & Genzel, R. 1987, *ApJ*, 316, 231
- Jaffe, D. T., & Plume, R. 1995, *ASP Conf. Ser.*, 73, 79

- Jansen, D. J., van Dishoeck, E. F., Keene, J., et al. 1996, *A&A*, 309, 899
- Kaufman, M. J., Wolfire, M. G., Hollenbach, D. J., et al. 1999, *ApJ*, 527, 795
- Kaifu, N. 1985, in *Int. Symp. on Mm and Submm Wave Radio Astronomy, Proceedings (A86-41201 19-88)*, Granada, Spain
- Keene, J., Lis, D., Philipps, T., et al. 1997, *Proc. IAU*, 178, 129
- Köster, B., Störzer, H., Stutzki, J., & Sternberg, A. 1994, *A&A*, 284, 54
- Kurucz, R. L. 1991, *Stellar atmospheres*, Schenectady (New York: L. Davis press), 441
- Langer, W. D., & Penzias, A. A. 1990, *ApJ*, 357, 477
- Little, L., Kelly, M., Habing, R., & Millar, T. 1995, *MNRAS*, 277, 307
- Loushin, R., Crutcher, R. M., & Bieging, J. H. 1990, *ApJ*, 362, L67
- Meixner, M., Haas, M., Tielens, A., et al. 1992, *ApJ*, 390, 499
- Mezger, P. G., Chini, R., Kreysa, E., & Wink, J. E. 1987, *A&A*, 182, 127
- Petitpas, G. R., & Wilson, C. D. 2001, *ESA SP-460*, ed. G. L. Pilbratt, & J. Cernicharo
- Pineau de Forêts, G., Roueff, E., & Flower, D. R. 1992, *MNRAS*, 258, 45
- Plume, R., Jaffe, D., Tatematsu, K., et al. 1999, *ApJ*, 512, 768
- Plume, R., Bensch, F., Howe, J. E., et al. 2000, *ApJ*, 539, L133
- Poglitsch, A., et al. 1991, *Intern. J. IR-mm Waves*, 12, 859
- Richer, J., Padman, R., Ward-Thompson, D., Hills, R. E., & Harris, A. I. 1993, *MNRAS*, 262, 839
- Schieder, R., Horn, J., Siebertz, O., et al. 1998, *SPIE*, 3357, 359
- Schneider, N., Stutzki, J., Winnewisser, G., et al. 1998, *A&A*, 338, 262
- Schneider, N., Simon, R., Kramer, C., Stutzki, J., & Bontemps, S. 2002, *A&A*, 384, 225
- Sekimoto, Y., Tatematsu, K., & Arikawa, Y. 1999, *Proc. of Star Formation 1999, Japan*, June 21–25, 1999, ed. T. Nakamoto (Nobeyama Radio Observatory), 86
- Simon, R., Stutzki, J., Sternberg, A., & Winnewisser, G. 1997, *A&A*, 327, L9
- Smith, N., Jones, T. J., Gehrz, R. D., et al. 2001, *ApJ*, 121, 984
- Staude, H., Lenzen, R., Dyck, H. M., & Schmidt, G. C. 1982, *ApJ*, 255, 95
- Stacey, G., Geis, N., Genzel, R., et al. 1991a, *ApJ*, 373, 423
- Stacey, G., Townes, C. H., Geis, N., et al. 1991b, *ApJ*, 382, L37
- Sternberg, A., & Dalgarno 1989, *ApJ*, 338, 197
- Stutzki, J., Ungerechts, H., & Winnewisser, G. 1982, *A&A*, 111, 201
- Stutzki, J., & Winnewisser, G. 1985, *A&A*, 144, 13
- Stutzki, J., Stacey, G., Genzel, R., et al. 1988, *ApJ*, 332, 279
- Tatematsu, K., et al., *Proc. of Star Formation 1999, Japan*, June 21–25, 1999, ed. T. Nakamoto (Nobeyama Radio Observatory), 72
- Tauber, J. A., Tielens, A., Meixner, M., et al. 1994, *ApJ*, 422, 136
- Tauber, J. A., Lis, D., Keene, J., et al. 1995, *ApJ*, 297, 567
- Tielens, A. G. G. M., & Hollenbach, D. J. 1985, *ApJ*, 291, 722
- van den Ancker, M., Tielens, A. G. G. M., & Wesselius, P. R. 2000, *A&A*, 358, 1035

Online Material

Appendix A: Determination of excitation conditions

From the observed [C II], [C I] 2→1, [C I] 1→0, and CO 7→6 and 4→3 lines, we determine the excitation conditions in an LTE analysis in the following way:

Excitation temperature and opacities from ¹²CO lines

Using the observed main beam brightness temperatures $T_{\text{mb}}(\text{CO } 7 \rightarrow 6)$ [K] and $T_{\text{mb}}(\text{CO } 4 \rightarrow 3)$ [K] and neglecting the cosmic background radiation at these high frequencies, we calculate the excitation temperatures T_{ex} assuming optically thick emission by:

$$\begin{aligned} T_{\text{ex}}(\text{CO } 7 \rightarrow 6) &= 38.7 \times [\ln(38.7/T_{\text{mb}}(\text{CO } 7 \rightarrow 6) + 1)]^{-1} [\text{K}] \\ T_{\text{ex}}(\text{CO } 4 \rightarrow 3) &= 22.1 \times [\ln(22.1/T_{\text{mb}}(\text{CO } 4 \rightarrow 3) + 1)]^{-1} [\text{K}]. \end{aligned} \quad (\text{A.1})$$

The excitation temperatures (see Fig. 11) derived in this way are different, $T_{\text{ex}}(\text{CO } 4 \rightarrow 3)$ is typically a factor 2 smaller than $T_{\text{ex}}(\text{CO } 7 \rightarrow 6)$ along the cut. This indicates that the cloud is not in LTE and the values for T_{ex} should be treated with care since they represent only lower limits of the kinetic temperature. In addition, we get some evidence (Sect. 3.4) that the CO 7→6 line may be optically thin.

Excitation temperature from the [C I] 2→1/1→0 ratio

In the optically thin regimes, and neglecting the cosmic background radiation, the column densities in the upper level of the [C I] 2→1 and 1→0 lines are proportional to the line integrated intensities $\int T_{\text{mb}}(\text{CI})dv$ (in [K km s⁻¹]):

$$\begin{aligned} N_{21} &= \frac{8\pi k\nu_{21}^2}{hc^3 A_{21}} \int T_{\text{mb}}([\text{C I}] 2 \rightarrow 1) dv \\ &= 4.72 \times 10^{15} \int T_{\text{mb}}([\text{C I}] 2 \rightarrow 1) dv [\text{cm}^{-2}] \quad \text{and} \\ N_{10} &= \frac{8\pi k\nu_{10}^2}{hc^3 A_{10}} \int T_{\text{mb}}([\text{C I}] 1 \rightarrow 0) dv \\ &= 5.96 \times 10^{15} \int T_{\text{mb}}([\text{C I}] 1 \rightarrow 0) dv [\text{cm}^{-2}]. \end{aligned} \quad (\text{A.2})$$

T_{mb} [K] is the main beam brightness temperature and A_{ul} the Einstein-A coefficients. The column densities ratio is then $\frac{N_{21}}{N_{10}} = \frac{g_{21}}{g_{10}} e^{-\frac{h\nu_{21}}{k_B T_{\text{ex}}}}$ with the statistical weights g . The excitation temperature is then calculated by

$$T_{\text{ex}} = \frac{h\nu_{21}}{k_B} \ln \left(\frac{N_{10} g_{21}}{N_{21} g_{10}} \right)^{-1} = \frac{38.8}{\ln(\frac{2.11}{R})} [\text{K}]. \quad (\text{A.3})$$

with $R = \int T_{\text{mb}}([\text{C I}] 2 \rightarrow 1) dv / \int T_{\text{mb}}([\text{C I}] 1 \rightarrow 0) dv$.

[C II] column density

We assume that the [C II] emission ($I([\text{C II}])$ in erg s⁻¹ sr⁻¹ cm⁻²) is optically thin or only marginally optically thick. Even though the [C II] line is bright in S 106, even stronger [C II] emission is

found in Orion, where spectrally resolved ¹²C⁺ and ¹³C⁺ data point towards an opacity of 0.75–1.85 (Stacey et al. 1991b). In addition, model calculations (Kaufman et al. 1999) typically give line center optical depths of 1. We presume that the density and temperature of the gas is high enough for thermalized emission ($n > n_{\text{cr}} = 3 \times 10^3 \text{ cm}^{-3}$, $T > 91 \text{ K}$). There is ample observational evidence to support this assumption, see, e.g., Harris et al. (1987), Graf et al. (1993), and van den Ancker et al. (2000). In this case, the expression to determine the [C II] column density

$$N([\text{C II}]) = \eta_c^{-1} 2.1 \times 10^{20} \exp(91/T) I([\text{C II}]) \times (1 + 2 \exp(-91/T) + n_{\text{cr}}/n) [\text{cm}^{-2}] \quad (\text{A.4})$$

simplifies to

$$N([\text{C II}]) = \eta_c^{-1} I([\text{C II}]) 6.3 \times 10^{20} [\text{cm}^{-2}]. \quad (\text{A.5})$$

The beam filling factor η_c is assumed to be unity so that the derived column densities are lower limits.

The optical depths of the [C I] 2→1 and 1→0 lines

The [C I] 1→0 optical depth is given by

$$\tau([\text{C I}] 1 \rightarrow 0) = -\ln(1 - T_{\text{mb}}([\text{C I}] 1 \rightarrow 0) \times (\exp(23.62/T_{\text{ex}}) - 1)/23.62) \quad (\text{A.6})$$

and the [C I] 2→1 optical depth by

$$\tau([\text{C I}] 2 \rightarrow 1) = -\ln(1 - T_{\text{mb}}([\text{C I}] 2 \rightarrow 1) \times (\exp(38.8/T_{\text{ex}}) - 1)/38.8) \quad (\text{A.7})$$

with the excitation temperature from Eq. (A.3) and the observed main beam brightness temperature $T_{\text{mb}}([\text{C I}])$ [K] of the atomic carbon lines.

The [C I] column density

The [C I] column density $N(\text{CI})$ [cm⁻²] is calculated using the integrated intensity $\int T_{\text{mb}}([\text{C I}] 1 \rightarrow 0) dv$ [K km s⁻¹] (Frerking et al. 1989). Again, a beam filling factor of 1 is assumed. The correction factor $\tau([\text{C I}])/(1 - \exp(-\tau([\text{C I}])))$ is applied if the optical depth of the [C I] 1→0 line is not much smaller than unity. T_{ex} is again determined from Eq. (A.3).

$$\begin{aligned} N(\text{CI}) &= 5.94 \times 10^{15} \times \tau([\text{C I}]) / (1 - \exp(-\tau([\text{C I}]))) \\ &\times \left[(1 + 3 \exp(-23.6/T_{\text{ex}}) \right. \\ &\quad \left. + 5 \exp(-62.4/T_{\text{ex}})) / 3 \exp(-23.6/T_{\text{ex}}) \right] \\ &\times \int T_{\text{mb}}([\text{C I}] 1 \rightarrow 0) dv [\text{cm}^{-2}]. \end{aligned} \quad (\text{A.8})$$